

The circulation pattern and day-night heat transport in the atmosphere of a synchronously rotating aquaplanet: Dependence on planetary rotation rate



S. Noda^{a,1,*}, M. Ishiwatari^{b,c}, K. Nakajima^d, Y.O. Takahashi^{a,c}, S. Takehiro^e, M. Onishi^{a,2}, G.L. Hashimoto^f, K. Kuramoto^{b,c}, Y.-Y. Hayashi^{a,c}

^a Department of Planetology, Kobe University, Kobe 657-8501, Japan

^b Division of Earth and Planetary Sciences, Hokkaido University, Sapporo 060-0810, Japan

^c Center for Planetary Science, Kobe University, Kobe 650-0047, Japan

^d Department of Earth and Planetary Sciences, Kyushu University, Fukuoka 819-0395, Japan

^e Research Institute for Mathematical Sciences, Kyoto University, Kyoto 606-8502, Japan

^f Department of Earth Sciences, Okayama University, Okayama 700-8530, Japan

ARTICLE INFO

Article history:

Received 29 September 2015

Revised 21 August 2016

Accepted 6 September 2016

Available online 1 October 2016

Keywords:

Astrobiology

Atmospheres, dynamics

Atmospheres structure

Extra-solar, planets

Meteorology

ABSTRACT

In order to investigate a possible variety of atmospheric states realized on a synchronously rotating aquaplanet, an experiment studying the impact of planetary rotation rate is performed using an atmospheric general circulation model (GCM) with simplified hydrological and radiative processes. The entire planetary surface is covered with a swamp ocean. The value of planetary rotation rate is varied from zero to the Earth's, while other parameters such as planetary radius, mean molecular weight and total mass of atmospheric dry components, and solar constant are set to the present Earth's values. The integration results show that the atmosphere reaches statistically equilibrium states for all runs; none of the calculated cases exemplifies the runaway greenhouse state. The circulation patterns obtained are classified into four types: Type-I characterized by the dominance of a day-night thermally direct circulation, Type-II characterized by a zonal wave number one resonant Rossby wave over a meridionally broad westerly jet on the equator, Type-III characterized by a long time scale north-south asymmetric variation, and Type-IV characterized by a pair of mid-latitude westerly jets. With the increase of planetary rotation rate, the circulation evolves from Type-I to Type-II and then to Type-III gradually and smoothly, whereas the change from Type-III to Type-IV is abrupt and discontinuous. Over a finite range of planetary rotation rate, both Types-III and -IV emerge as statistically steady states, constituting multiple equilibria. In spite of the substantial changes in circulation, the net energy transport from the day side to the night side remains almost insensitive to planetary rotation rate, although the partition into dry static energy and latent heat energy transports changes. The reason for this notable insensitivity is that the outgoing longwave radiation over the broad area of the day side is constrained by the radiation limit of a moist atmosphere, so that the transport to the night side, which is determined as the difference between the incoming solar radiation and the radiation limit, cannot change greatly.

© 2016 The Authors. Published by Elsevier Inc.

This is an open access article under the CC BY license (<http://creativecommons.org/licenses/by/4.0/>).

1. Introduction

A number of recent systematic surveys have discovered many earth-sized exoplanets (e.g., Torres et al., 2015). Many of those

planets exist inside the tidal lock radius of their central stars, and are thought to be synchronously rotating (e.g., Von Bloh et al., 2007). Even when the global mean incoming heat flux from the central star is comparable to that of the present Earth's, the incident flux on the perpetual day side of a synchronously rotating planet can easily exceed the radiation limit of a moist atmosphere, which is the upper limit of outgoing longwave (infrared) radiation at the top of the atmosphere (OLR) defined by a one-dimensional radiative-convective equilibrium model of an atmosphere with a sufficient amount of liquid water on its bottom surface (Nakajima et al., 1992). So, a synchronously rotating planet may

* Corresponding author. Fax: +81 75 753 3715.

E-mail address: noda@gfd-dennou.org (S. Noda).

¹ Present address: Division of Earth and Planetary Sciences, Kyoto University, Kyoto 606-8502, Japan

² Present address: Department of Earth Sciences, Okayama University, Okayama 700-8530, Japan

<http://dx.doi.org/10.1016/j.icarus.2016.09.004>

0019-1035/© 2016 The Authors. Published by Elsevier Inc. This is an open access article under the CC BY license (<http://creativecommons.org/licenses/by/4.0/>).

easily enter the runaway greenhouse state if the day side to night side (hereafter, day–night) energy transport is insufficient.

However, in previous studies on atmospheres of synchronously rotating planets using general circulation models (GCMs), the runaway greenhouse state does not emerge for several different values of planetary rotation rate with the present value of the Earth's solar constant (e.g., Joshi, 2003; Merlis and Schneider, 2010; Edson et al., 2011). Even with the a solar constant 1.9 times that of the Earth, Yang et al. (2013) obtains statistically equilibrium states in an aquaplanet GCM experiment, in which high cloud albedo in the regions around the subsolar point presumably prevents a runaway greenhouse state. These results suggest that the mechanism that determines the amount of day–night energy transport still remains to be understood and its dependence on planetary rotation rate to be revealed. These issues may be crucial in considering the habitability of synchronously rotating exoplanets.

The atmospheric circulation structure, which should be related to day–night energy transport, has been shown to depend on the planetary rotation rate (e.g., Showman et al., 2013), which is, in this paper, represented by Ω^* , the value divided by that of the present Earth: $7.272 \times 10^{-5} \text{ s}^{-1}$. Using a GCM with a slab ocean, Merlis and Schneider (2010) obtains a day–night thermally direct circulation in the case with $\Omega^* = 1/365$, whereas high-latitude westerlies emerge in the case with $\Omega^* = 1$. The latter circulation pattern is similar to that obtained earlier by Joshi (2003) with $\Omega^* = 1$. Merlis and Schneider (2010) names the two circulation regimes the “slowly rotating regime” and the “rapidly rotating regime”, respectively. However, there is little information on the transition between these two regimes. Edson et al. (2011) explores the Ω^* dependence of the atmospheric circulation structures of both dry and moist planets, and shows that, in addition to the two regimes similar to those identified by Merlis and Schneider (2010), a regime with a strong westerly zonal wind in low latitudes appears with intermediate values of Ω^* . It is also shown that, for the dry planet condition, an abrupt change of zonal wind velocity occurs and multiple equilibria with hysteretic behavior exist between $\Omega^* = 0.109$ and $\Omega^* = 0.25$. However, corresponding multiple equilibria for the aquaplanet have not been described clearly.

As for day–night energy transport, Merlis and Schneider (2010) shows that the amounts of moist static energy transport are almost the same for the two cases with $\Omega^* = 1/365$ and $\Omega^* = 1$, but there is no information about energy transport for intermediate values of Ω^* . Edson et al. (2011) describes Ω^* dependences of minimum, maximum, and globally averaged mean surface temperature, but does not present that of energy transport. The dependence of day–night energy transport on Ω^* , together with possible constraints on it, remain to be explored.

Recently, GCM experiments have also been performed in order to examine possible climates on synchronously rotating terrestrial exoplanets with particular parameter setups estimated from observations (e.g., Heng and Vogt, 2011; Wordsworth et al., 2011). Naturally, detailed parameter dependence is not examined in these works, since they focus on exploration of climates for the parameters of particular exoplanets.

In this paper, a series of GCM runs with Ω^* incremented by small steps is performed under a simple setup considering a moist planet that rotates synchronously. We will attempt to confirm that, for the same value of incoming solar flux as that of the present Earth's, statistically equilibrium states are obtained and the runaway greenhouse state does not occur for various values of Ω^* including those that are not closely examined in the previous studies. We also examine how Ω^* affects the atmospheric circulation structure and day–night energy transport, and consider what determines the amount of day–night energy transport. The same simple model configuration as used in Ishiwatari et al. (2002) and Ishiwatari et al. (2007) is adopted, namely cloud-free conditions,

gray radiation, swamp ocean and so on. This choice allows us to compare the results of the experiment directly with our previous studies showing that the three-dimensional moist atmosphere evolves into the runaway greenhouse state when the global mean insolation exceeds the radiation limit. Using the swamp condition allows the system to reach a statistically equilibrium state in a shorter time than with a slab ocean, and is convenient for execution of a large number of runs with various Ω^* and initial conditions. Varying these initial conditions is necessary to search for possible multiple equilibrium solutions.

The specification of the GCM and the experimental setups are described in Section 2. The realization of statistically equilibrium states is confirmed, and an overview of the dependence of the structure of the atmospheric circulation on Ω^* are given in Section 3. Four typical cases with different values of Ω^* are chosen and their associated structures of atmospheric circulation are described in Section 4. The dependence of day–night energy transport on Ω^* is analyzed, and it is argued that day–night energy transport is constrained by the radiation limit of a moist atmosphere in Section 5. Discussions and conclusions are given in Section 6.

2. Model and experimental setup

The GCM utilized in this study is DCPAM5 (the Dennou-Club Planetary Atmospheric Model, <http://www.gfd-dennou.org/library/dcpam/index.htm.en>), which is reconstructed from GFD-Dennou-Club AGCM5 used in Ishiwatari et al. (2002) and Ishiwatari et al. (2007) with a design convenient for numerical experiments on various planetary atmospheres. With DCPAM5, it is confirmed that the runaway greenhouse state emerges under the same conditions as those of Ishiwatari et al. (2002). Here we use the same model configuration as that of Ishiwatari et al. (2002). The governing equations for dynamical processes are the primitive equations. Simple parameterization schemes are adopted for physical processes. The atmosphere consists of water vapor and dry air. Both dry air and water vapor are transparent to shortwave radiation, and only water vapor absorbs longwave radiation with constant absorption coefficient ($0.01 \text{ m}^2 \text{ kg}^{-1}$). The moist convective adjustment scheme (Manabe et al., 1965) is used as a cumulus parameterization. Condensed water is immediately removed from the atmosphere as rain. There is no cloud; absorption and scattering of radiation by clouds are not incorporated. The surface of the planet is entirely covered with the swamp ocean, an ocean with zero heat capacity. It is assumed that the ocean does not transport heat horizontally and does not freeze. The surface albedo is set to zero. A bulk formula (Louis et al., 1982) is used for surface flux calculation.

In order to draw on existing knowledge of the present Earth's atmosphere, the values of parameters used in our experiment are basically those of the Earth except for planetary rotation rate and obliquity. The values of molecular weight and specific heat of dry air are set to $28.964 \times 10^{-3} \text{ kg mol}^{-1}$ and $1004.6 \text{ J K}^{-1} \text{ kg}^{-1}$, respectively. The values of molecular weight and specific heat of water vapor are set to $18.0 \times 10^{-3} \text{ kg mol}^{-1}$ and $1810.0 \text{ J K}^{-1} \text{ kg}^{-1}$, respectively. The planetary radius R_p is set to $6.371 \times 10^3 \text{ km}$. The acceleration of gravity is 9.80665 m s^{-2} , and global mean surface pressure is 10^5 Pa . The synchronously rotating planet is configured with the obliquity set to zero, and the distribution of solar incident flux fixed to the planetary surface (Fig. 1) according to

$$S_{\text{solar}} = S_0 \max[0, \cos \phi \cos(\lambda - \lambda_0)], \quad (1)$$

where ϕ is latitude and λ is longitude, with subsolar longitude $\lambda_0 = 90^\circ$ and solar constant $S_0 = 1380 \text{ W m}^{-2}$, which is about 88% of the threshold value ($S_0 = 1570 \text{ W m}^{-2}$) to enter the runaway greenhouse state obtained by the non-synchronously rotating aquaplanet experiment by Ishiwatari et al. (2002). We use 16 values of Ω^* : $\Omega^* = 0, 0.05, 0.1, 0.15, 0.2, 0.25, 0.33, 0.5, 0.6,$

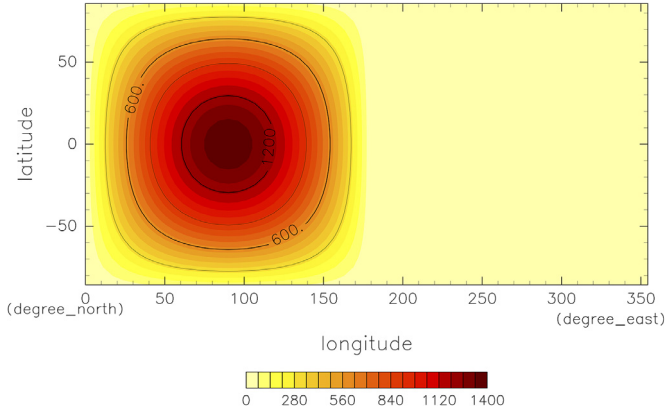


Fig. 1. Horizontal distribution of the incident solar flux [W m^{-2}] given by Eq. (1). Contour interval is 300 W m^{-2} .

0.67, 0.7, 0.75, 0.8, 0.85, 0.9, and 1. Hereafter each case will be referred to as character Ω followed by the value of Ω^* . For example, $\Omega 0.05$ is the case with orbital period of 20 Earth days. Note that changing Ω^* with fixed solar constant means changing the luminosity of the central star. Although no planet with $\Omega^* = 0$ exists in reality, we examine the circulation structure of this idealized non-rotating planet as the limiting case of small Ω^* .

For the horizontal discretization, we use the spherical spectral transform method with triangular truncation at total wavenumber 21 (T21), giving 64 grid-points for the longitudinal axis and 32 grid-points for the latitudinal axis. As the vertical coordinate, $\sigma \equiv p/p_s$ is adopted, where p_s is surface pressure. The number of vertical levels is set to 16. The model top level is set to $\sigma = 0.02$. We performed test runs for several values of Ω^* employing 32 vertical levels with the top level of $\sigma = 9.2 \times 10^{-5}$. The results show no qualitative change in either the atmospheric circulation characteristics or the energy budget compared with those with 16 vertical levels; the change in day side averaged OLR is at most 10 W m^{-2} (figures not shown), which is negligibly small compared to the value of OLR itself. We also conducted a high resolution test experiment up to T341 with $\Omega^* = 1$, and confirmed that the large scale circulation and the surface temperature patterns are mostly unchanged. These sensitivity tests show that the vertical and horizontal resolutions are adequate for the present purpose. Some aspects of the resolution dependence are demonstrated later in Appendix A.

For each Ω^* , we perform 10 runs. As will be discussed in the following sections, we have recognized that initial condition dependence appears for certain values of Ω^* ; different types of circulation patterns result from slightly different initial conditions. The initial condition for each run is an isothermal (280K) resting atmosphere with a small temperature perturbation in the form of random noise with amplitude of 0.1 K added to all grid-points; we prepare ten different perturbation fields for the ten runs. Each run is integrated for 2000 Earth days, and the data from the last 1000 days are used for analysis.

3. Dependence of atmospheric circulation characteristics on planetary rotation rate

In all runs the atmosphere reaches a statistically equilibrium state; the runaway greenhouse state does not emerge. Fig. 2 shows temporal changes of the global mean values of surface temperature and OLR obtained in four typical runs with different values of Ω^* . In every case, the atmosphere settles down after about 300 days to a statistically equilibrium state in which both global mean sur-

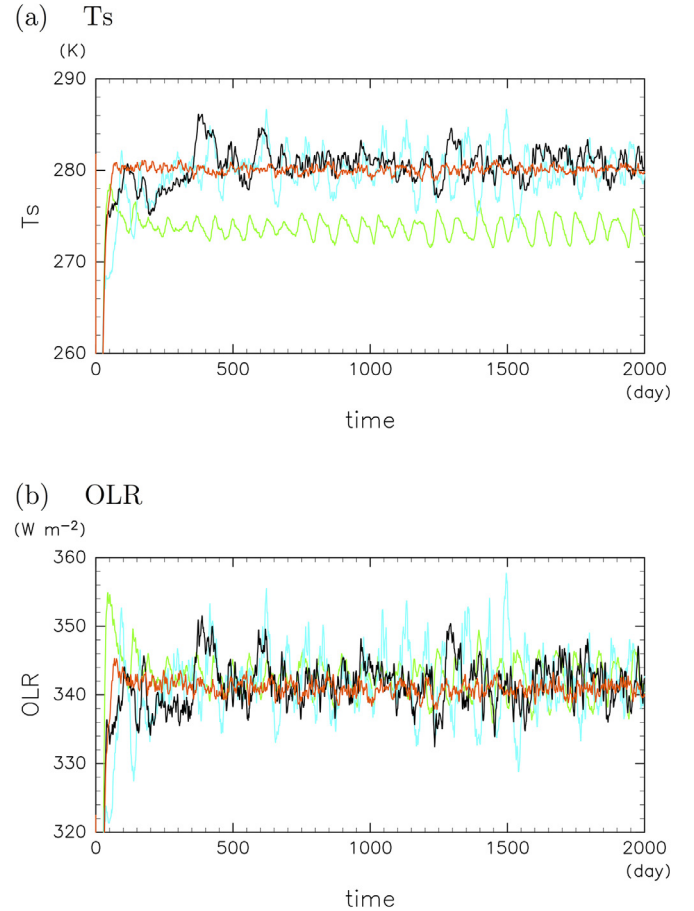


Fig. 2. Time series of global mean quantities. (a) Surface temperature [K] and (b) OLR [W m^{-2}]. Green, light-blue, black, and red lines indicate $\Omega 0.0$, $\Omega 0.15$, $\Omega 0.75$, and $\Omega 1.0$, respectively. (For interpretation of the references to colour in this figure legend, the reader is referred to the web version of this article.)

face temperature and OLR fluctuate around their equilibrium values. The temporal mean values of global mean surface temperature and the magnitudes of temperature fluctuation differ among runs.

The structure of the atmospheric circulation varies with Ω^* . Fig. 3 summarizes the variety of global distributions of time mean surface temperature for various values of Ω^* . For each value of Ω^* , the result of a single run arbitrarily chosen from the ten runs is plotted. In Fig. 3, we can identify at least three features that characterize the variety of surface temperature. First, an equatorial warm belt in the night hemisphere is present in $\Omega 0.05 - \Omega 0.8$ (Fig. 3b–m), while it is absent in the other cases. Second, the equatorial region is generally warmer in $\Omega 0.0 - \Omega 0.8$ (Fig. 3a–m), while the mid-latitude regions are warmer in the other cases. These two features above reflect the meridional structures of zonal mean zonal wind, as will be shown later. Third, a north-south asymmetry is evident in $\Omega 0.6 - \Omega 0.8$ (Fig. 3i–m), while it is absent or weak in the other cases. This last feature reflects the presence of north-south asymmetric variability with long time scales, as will be described in Section 4.3.

For a more quantitative description of the general dependence of the atmospheric circulation structure on Ω^* , bearing in mind the three features of the surface temperature fields identified above, we examine the Ω^* -dependences of four quantities. These are the surface temperatures at the subsolar and antisolar points, the upper tropospheric zonal mean zonal wind at the equator, and a measure of north-south asymmetry in the surface temperature

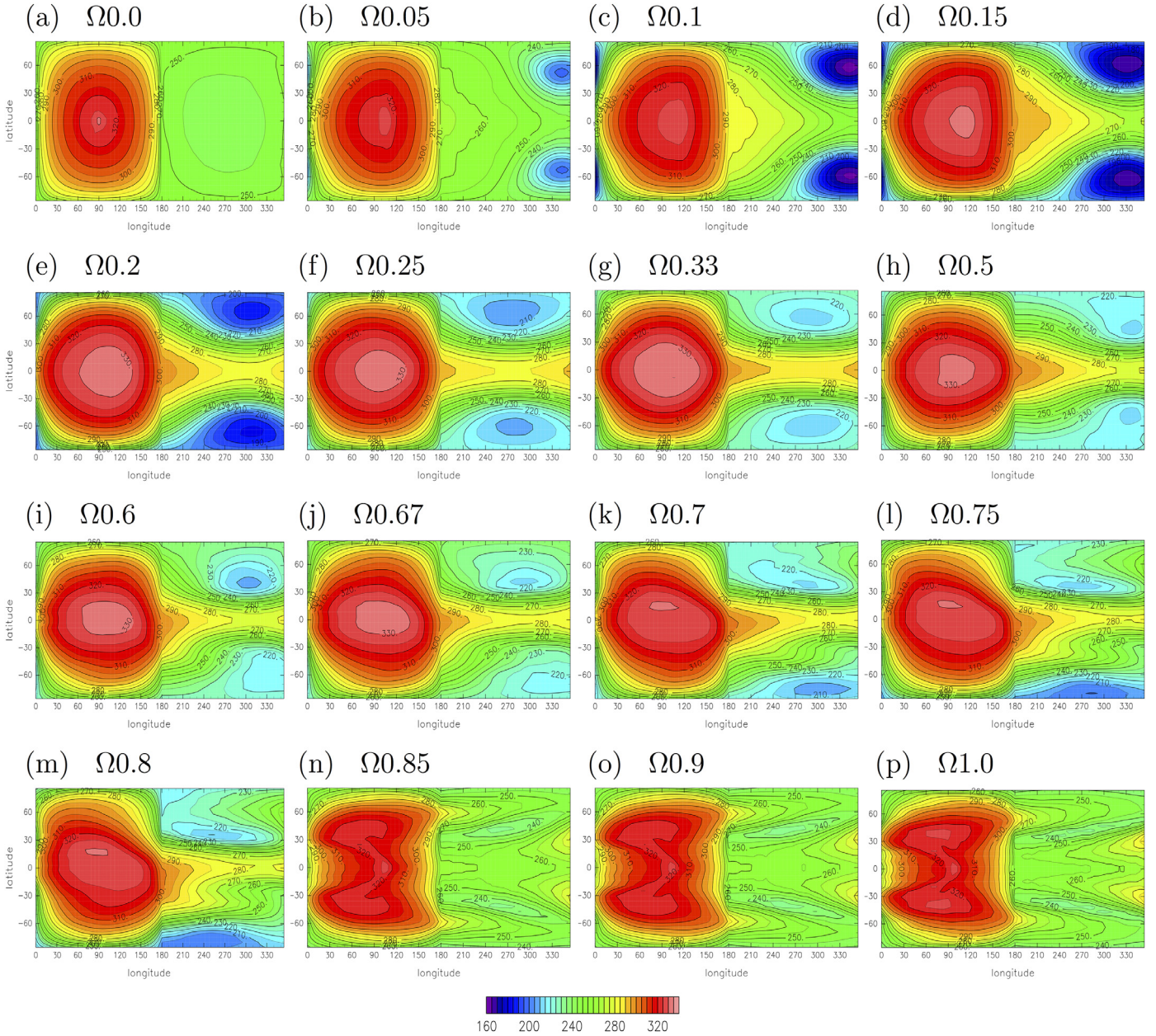


Fig. 3. Horizontal distributions of 1000-day mean surface temperature for all of the computed values of Ω^* . Contour interval is 5 K.

with short time scale transients filtered out defined by

$$\Delta_{NS}[T_s] \equiv \frac{1}{2\pi} \int_0^{\pi/2} \int_0^{2\pi} |\overline{\tilde{T}_s(\lambda, \phi)} - \overline{\tilde{T}_s(\lambda, -\phi)}| d\lambda \cos\phi d\phi, \quad (2)$$

where \tilde{T}_s is the 50 day running average of surface temperature, and the overbar means the temporal average over 1000 days. Fig. 4 shows the Ω^* dependences of these four quantities. Note that the ten runs for each value of Ω^* are plotted separately. Now we can identify two separate branches of atmospheric states: one extending from $\Omega^* = 0$ to $\Omega^* = 0.8$ (hereafter, the small- Ω branch), and the other from $\Omega^* = 0.7$ to $\Omega^* = 1$ (hereafter, the large- Ω branch). Between $\Omega^* = 0.7$ and $\Omega^* = 0.8$, these two branches coexist, giving multiple equilibria. The preference between the two branches in the range of the multiple equilibria seems to depend on the value of Ω^* ; the ratio of runs on the large- Ω branch increases from 10% for $\Omega^* = 0.7$ to 80% for $\Omega^* = 0.8$. The branch taken by a particular run depends on small differences in the initial conditions. It is determined in the first ~ 500 days of the model integration,

and there is no switching to the other branch after that. Note that those shown in Fig. 3k–m belong to the small- Ω branch by chance; there are also runs belonging to the large- Ω branch for this range of Ω^* , with surface temperature structure similar to those shown in Fig. 3n–p.

In Fig. 4 we observe that the atmospheric circulation characteristics change continuously but markedly on the small- Ω branch. When $\Omega^* = 0$, both zonal mean zonal wind and north-south asymmetry are negligible. As Ω^* increases, the westerly wind intensifies rapidly, and the night side surface temperature rises rapidly, both of which are tied to the appearance of the equatorial warm belt identified in Fig. 3b–m. The temperature at the subsolar point falls at first, then rises. The north-south asymmetry remains small. Around $\Omega^* = 0.5$, the north-south asymmetry increases, and continues to increase with increase of Ω^* . The asymmetry has been identified in Fig. 3i–m, but is not evident in cases $\Omega 0.2$ – $\Omega 0.5$ (Fig. 3e–h), where, as will be shown later, the temporal scale of the variability is short compared with the averaging period of

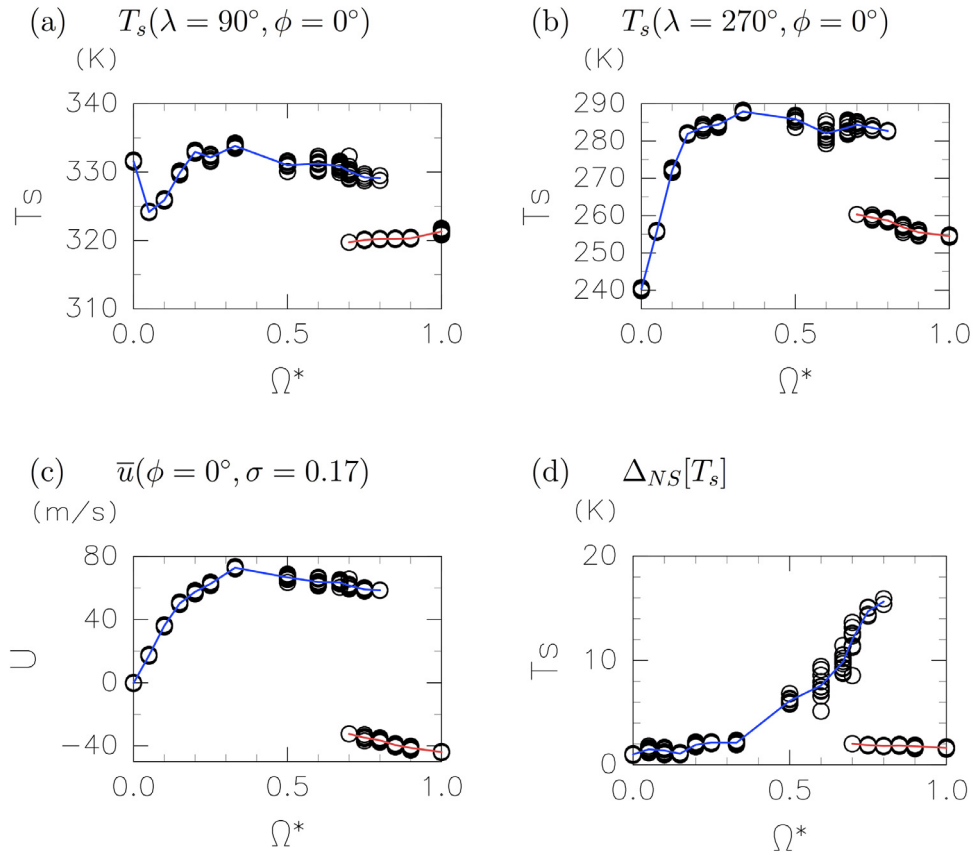


Fig. 4. Ω^* dependences of (a) surface temperature [K] at the subsolar point, (b) surface temperature [K] at the antipolar point, (c) zonal mean equatorial zonal wind [m s^{-1}] at $\sigma = 0.17$, and (d) degree of north-south asymmetry of surface temperature defined by Eq. 2 in the text [K]. The values are temporal averages between day 1000 and day 2000. All 10 runs for each Ω^* case are plotted. Red and blue lines are ensemble averages for the small- Ω^* and the large- Ω^* branches, respectively. (For interpretation of the references to colour in this figure legend, the reader is referred to the web version of this article.)

1000-days. Until the end of the small- Ω^* branch at $\Omega^*=0.8$, the values of temperature at the subsolar and antipolar points remain high, and the zonal mean wind at the equator maintains its strength. On the large- Ω^* branch, the upper tropospheric zonal mean wind is easterly. The temperature is lower than that of the small- Ω^* branch at both the subsolar and antipolar points, and north-south asymmetry is weak. Changes in the four circulation characteristics are rather small over the entire range ($0.7 \lesssim \Omega^* \lesssim 1$) of the large- Ω^* branch.

4. Typical atmospheric circulation structures

In order to understand the atmospheric circulation and its dependence on Ω^* on the synchronously rotating planet, we examine here the spatial structures and temporal variation of the solutions in detail. Although the circulation structure changes more or less continuously as Ω^* changes on the small- Ω^* branch as implied in Figs. 3 and 4, we can classify the circulation structures into three types according to the zonal wind structure and the temporal variability. They are, in order of the planetary rotation rate where they appear, Type-I, characterized by day-night convection, Type-II, characterized by a broad equatorial westerly jet and a north-south symmetric stationary wave-like pattern that turns out to be a stationary Rossby wave, and Type-III, characterized by long time scale north-south asymmetric variability. In the large- Ω^* branch we can classify the circulation structure as Type-IV, characterized by a pair of mid-latitude deep westerly jets. For each of the four types, we choose one case and examine it in detail below.

4.1. Type-I: day-night convection (case $\Omega 0.0$)

The Type-I circulation appears in cases with very small values of Ω^* , and is characterized by day-night convection; it is similar to those obtained with small Ω^* in earlier studies (Edson et al., 2011; Merlis and Schneider, 2010). We examine case $\Omega 0.0$ as a representative case of Type-I.

The time mean structure of the atmospheric circulation in case $\Omega 0.0$ is shown in Fig. 5. Upper tropospheric horizontal flow diverges toward the night side (Fig. 5b) from the concentrated upward motion at the subsolar point, where intense precipitation develops (Fig. 5e). The outflow is strong not only in the upper troposphere ($\sigma \sim 0.23$) but also at the middle levels around $\sigma \sim 0.55$ (Fig. 5c). In the middle troposphere, the entire planet except at the subsolar point is covered with a widespread, weak, and almost homogeneous downward flow (Fig. 5c). In the lower troposphere ($\sigma \sim 0.9$), the air flow diverges from the antipolar point and returns to the day side, connected to the flow converging toward the subsolar point.

The surface temperature distribution (Fig. 5h) closely follows the incident solar flux distribution (Fig. 1). The night side surface temperature is almost homogeneous; its variation is as small as 10 K, being by far the smallest among all the experiments. The surface pressure distribution (Fig. 5a) can be interpreted as a direct response to the surface temperature distribution; a notable feature is the heat low in the lower troposphere of the day side (Fig. 5a and c). Temperature on the night side is generally highest in the middle levels ($\sigma \sim 0.6$) and lower nearer the surface (Fig. 5c). In contrast, temperature in the heat low around the subsolar point ($20^\circ \leq \lambda \leq 160^\circ$), increases with decreasing altitude.

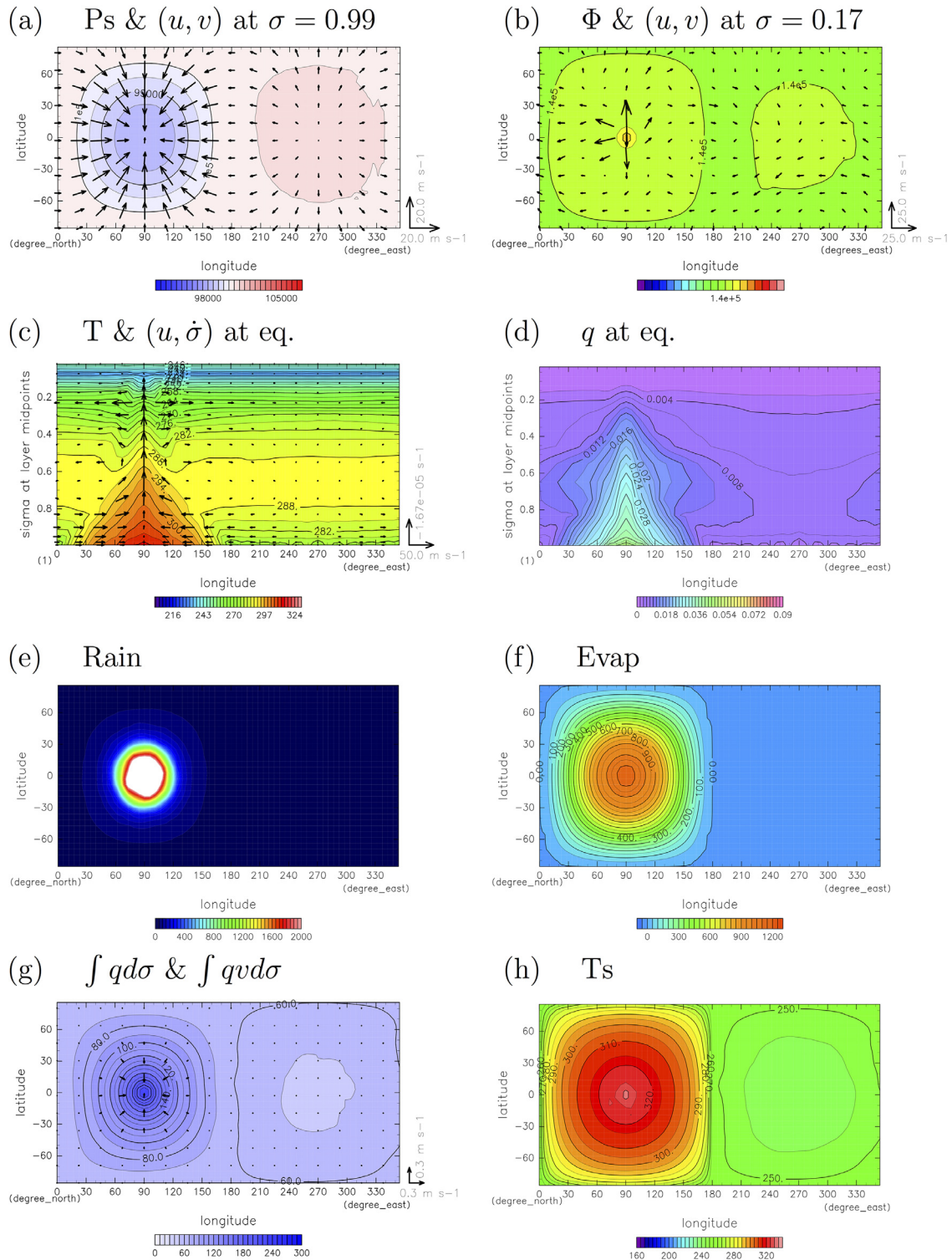


Fig. 5. Day 1000 to day 2000 temporal mean fields for case $\Omega 0.0$. (a) Surface pressure (color shading) [Pa] and horizontal wind vectors [m s^{-1}] at the lowest level. Contour interval of surface pressure is 5×10^2 Pa, and the unit vectors of zonal and meridional wind are 20 m s^{-1} . (b) Horizontal wind vector [m s^{-1}] and geopotential [J kg^{-1}] at $\sigma = 0.17$. Unit vector indicates 25 m s^{-1} . Contour interval of geopotential is 500 J kg^{-1} . (c) Vertical wind $-\sigma$ [s^{-1}] and zonal wind [m s^{-1}] (vector), and temperature [K] (color) in the equatorial vertical section. Unit vectors of vertical wind and zonal wind are $1.67 \times 10^{-5} \text{ s}^{-1}$ and 50 m s^{-1} , respectively. Contour interval of temperature is 5 K . (d) Specific humidity at the equator. Contour interval is 2×10^{-3} . (e) Condensation heating [W m^{-2}]. Color interval is 50 W m^{-2} . White area represents heating over 2000 W m^{-2} . (f) Horizontal distribution of surface evaporation [W m^{-2}]. Color interval is 50 W m^{-2} . (g) Vertically integrated water vapor flux [m s^{-1}] and vertically integrated water vapor mass [kg m^{-2}]. Unit vector is 0.3 m s^{-1} . Contour interval is 10 kg m^{-2} . (h) Surface temperature [K]. Contour interval is 5 K . (For interpretation of the references to colour in this figure legend, the reader is referred to the web version of this article.)

The hydrological cycle is governed by the direct day-night circulation. Surface evaporation has its maximum at the subsolar point, and is very small over the whole night side (Fig. 5f). Rainfall occurs almost exclusively around the subsolar point (Fig. 5e). The middle level outflow from the subsolar point (Fig. 5c) advects moist air into the night side, producing relatively moist tongues ($0.45 \leq \sigma \leq 0.65$, $\lambda < 210^\circ$ and $\lambda > 320^\circ$) (Fig. 5d). However, the magnitude of the vertically integrated water vapor flux (Fig. 5g) is fairly small compared to those for the other circulation types.

4.2. Type-II: stationary Rossby wave on broad equatorial westerly jet (case $\Omega 0.15$)

The Type-II atmospheric circulation structure appears for $0.05 \leq \Omega^* \leq 0.2$ and is characterized by a warm region on the night side (Fig. 3b–d) below an intense broad equatorial westerly wind as shown in Fig. 4c, and large amplitude wavenumber one stationary waves in the higher latitudes. These features are also seen in the circulations obtained in an intermediate range of Ω^* by Edson et al. (2011). We examine case $\Omega 0.15$ as a representative case of Type-II.

The time mean structure of the atmospheric circulation in case $\Omega 0.15$ is shown in Fig. 6. The most notable feature is the emergence of a broad and deep westerly wind that covers almost the whole depth of the troposphere (Fig. 6c) of the low-latitude region (Fig. 6b). In the bottom layer near the surface, a trace signature of day-night circulation can still be noted (Fig. 6a). The location of maximum rainfall and the associated deep updraft are shifted eastward from the subsolar point by about 20° (Fig. 6c and e), possibly due to moisture advection by the deep westerly wind. The surface temperature peak is also shifted eastward from the subsolar point by 25° (Fig. 6h). A similar eastward shift emerges also in the other cases on the small Ω branch, explaining the drop in subsolar point surface temperature at $\Omega^* \sim 0$ (Fig. 4a). The peak of evaporation remains at the subsolar point (Fig. 6f). In fact, the latent heat flux around the equator on the day side changes little over the range of Ω^* examined in this study. The insensitivity to Ω^* results from the employment of the swamp surface condition and cloud free condition; the incoming shortwave radiation reaching the ground surface has fixed geographical distribution, and must be approximately balanced by the energy loss by latent heat of evaporation. The surface pressure minima are located at $(\lambda, \phi) \sim (120^\circ, \pm 15^\circ)$; these are not only to the east of the subsolar point, but also off the equator (Fig. 6a). The higher-latitude regions are characterized by intense wavenumber one stationary waves manifested as the ridge around $\lambda \sim 150^\circ$ and the cyclones around $(\lambda, \phi) \sim (330^\circ, \pm 60^\circ)$ (Fig. 6b). The pressure signatures are generally geostrophic, and have an equivalent barotropic vertical structure suggested by the low surface pressure signatures below the upper level low pressure area (Fig. 6a).

The deep, broad equatorial westerly wind transports a large amount of sensible and latent heat to the night side, which is manifested as the warm and moist tongue in the lower to the middle troposphere extending eastward crossing the terminator at $\lambda = 180^\circ$ (Fig. 6c and d). A considerable portion (about one fourth) of the water vapor transported to the night side at $\lambda = 180^\circ$ returns to the day side at $\lambda = 360^\circ$ (figure not shown). At $\lambda = 180^\circ$, water vapor transport to the night side is more intense in the high-latitude regions than in the equatorial region, resulting from the meandering of the eastward wind associated with the intense wavenumber one stationary waves and near surface westward wind near the equator. Rainfall is no longer focused at the subsolar point, as it is associated with the moisture transport, and some amount of rainfall occurs even in the night hemisphere (Fig. 6e) despite the negligibly small amount of surface evaporation. Also due to the enhanced water vapor transport, the column integrated

moisture content around the antisolar point reaches about three times that in case $\Omega 0.0$ (Fig. 6g). Actually, column integrated moisture content increases considerably also on the day side; the peak value near the subsolar point in case $\Omega 0.15$ is about 1.5 times the value of that in case $\Omega 0.0$, and its associated greenhouse effect results in the rise of surface temperature following the drop near $\Omega^* \sim 0$ (Fig. 4a).

It is notable that the horizontal distribution of surface temperature closely follows that of column moisture content on the night side (Fig. 6g and h); in an extensive region of high column water vapor content in the low latitudes, surface temperature is high, whereas it is very low in the dry regions located around the low pressure centers of wavenumber one structure at higher latitudes. The energy budget at the ground surface explains this close relationship; because incident solar flux is absent and both latent ($\sim 2 \text{ W m}^{-2}$) and sensible ($\sim -4 \text{ W m}^{-2}$) heat fluxes are negligibly small on the night side, the upward thermal radiation flux ($\sim 230 \text{ W m}^{-2}$) at the surface almost balances the downward long-wave radiation from the atmosphere that is exclusively emitted by water vapor, the only radiatively active component in this model.

When all Type-II cases are compared, the broad equatorial jet is stronger for the cases with larger value of Ω^* as indicated in Fig. 7, where the values of mass weighted global mean zonal wind velocity in Type-II are shown. Moreover, for $\Omega^* \geq 0.2$, the wind speed is close to the absolute values of the intrinsic phase speed of the normal mode Rossby wave of Longuet-Higgins (1968). The thin line in Fig. 7 shows the intrinsic phase speed of the meridionally gravest normal mode Rossby wave with wave number one, which we calculate with the spectral method of Kasahara (1976). Considering the vertical structure of the waves appearing in Type-II, we assume an equivalent depth of 10000 m, which is the value for the barotropic mode in an isothermal atmosphere of 245 K. The rough coincidence of the speed of the broad eastward equatorial jet and that of the intrinsically westward propagating normal mode Rossby wave for each Ω^* suggests that the wavenumber one planetary scale stationary wave in Type-II is resonantly excited on the broad westerly jet. Other evidence for the resonant excitation is the Ω^* -dependence of the amplitude and phase of the stationary wavenumber one waves. The cyclonic regions associated with the waves are expressed as the north-south symmetric cold regions in the night side mid to high latitudes (Fig. 3). For Ω^* from 0.05 to 0.2, the amplitude of the cyclonic regions is generally large. The longitudinal phase difference between the precipitation maximum and the cyclonic centers is about 270° for $\Omega^* = 0.05$. This is the largest eastward phase shift of the upper Rossby wave response to a wavenumber one thermal forcing in a westerly flow faster than the resonant speed. As Ω^* increases, the phase difference decreases, dropping below 180° for $\Omega^* = 0.25$ and 0.33. Possible mechanisms for the acceleration of the broad westerly wind and its resonant relation to the normal mode Rossby waves will be discussed in more detail in Section 6.3, referring to earlier studies.

For $\Omega^* \geq 0.25$, the westerly wind does not reach the normal mode Rossby wave speed. Our preliminary analysis reveals that, in these cases, mid-latitude transient disturbances, which may originate from baroclinic instability given the development of meridional temperature gradient (not shown), transport westerly momentum poleward and decelerate the broad westerly jet. Detailed analysis on the nature of the transient disturbances and their possible role as the “governor” of the equatorial jet remains to be performed.

4.3. Type-III: long time scale north-south asymmetric variability (case $\Omega 0.75$)

The Type-III atmospheric circulation structure appears on the small- Ω branch for $0.5 \leq \Omega^* \leq 0.8$. The temporally averaged

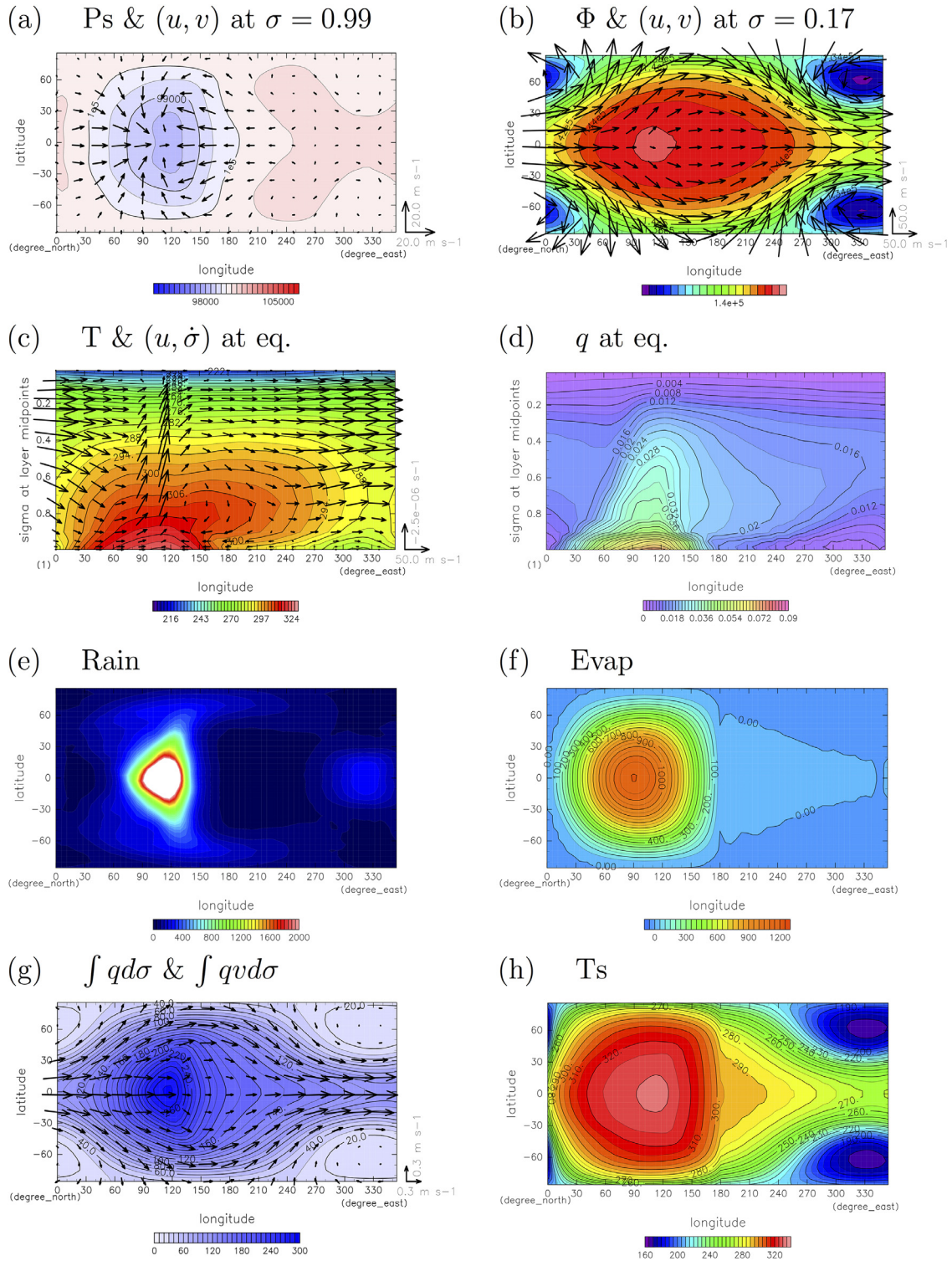


Fig. 6. Same as Fig. 5 but for case $\Omega_{0.15}$, except that the unit vector in (b) is 50 m s^{-1} and the unit vector of vertical wind in (c) is $2.5 \times 10^{-6} \text{ s}^{-1}$.

characteristics of Type-III are similar to those of Type-II in terms of the strong eastward equatorial jet, but, as shown in Fig. 4d, differ in the presence of significant north-south asymmetric long time scale variability.

Before considering the Type-III circulation structure in detail, we summarize the Ω^* dependences of the amplitude and the typical oscillation period of the north-south asymmetric variability. Fig. 8 compares the time series of zonal mean surface pressure in

four cases with different values of Ω^* . In case $\Omega_{0.2}$, where Type-II structure develops, a quasi periodic oscillation with amplitude of $\sim 20 \text{ hPa}$ and a temporal scale of $\sim 10 \text{ days}$ is notable. In case $\Omega_{0.5}$, in addition to an oscillation with $\sim 20 \text{ day}$ period, a slower, north-south asymmetric variability is evident; its period and amplitude are $\sim 40\text{--}100 \text{ days}$ and $\sim 45 \text{ hPa}$, respectively. In cases with larger Ω^* , the slow, north-south asymmetric variability is more intense and its characteristic period is longer; in case $\Omega_{0.67}$, the

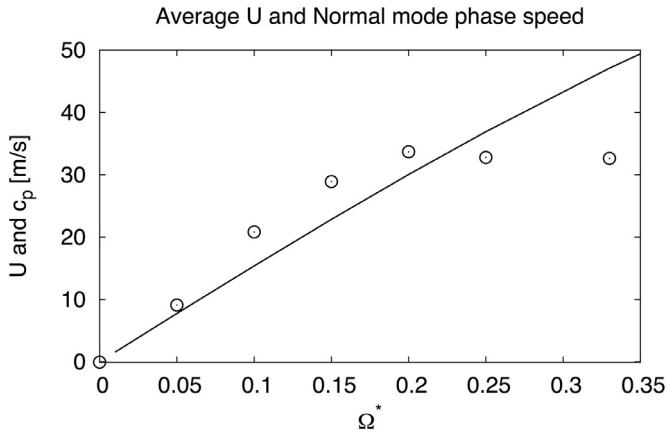


Fig. 7. Mass weighted global mean zonal wind velocity for cases with Ω^* from 0.0 to 0.33 (circles). Absolute value of westward phase velocity of the zonal wavenumber one gravest Rossby normal mode is indicated by the thin line for comparison.

amplitude is ~ 80 hPa, and the period is ~ 1000 days. In case $\Omega 0.75$, the amplitude is as large as ~ 160 hPa, and, looks almost permanent in Fig. 8d. However, by conducting several extended experiments, we have confirmed that the asymmetry does change its sign over a long time; the pressure deviation reverses at around $t = 25000$ days for the run shown in Fig. 8d. Furthermore, the sign of the asymmetry is determined by chance; in the ten runs conducted for $\Omega 0.75$, Type-III structure appears in four runs (not shown), and, during the period shown in Fig. 8d, two of them have a positive pressure anomaly in the northern high latitudes, and the remaining two are negative. We conclude that, despite the development of the distinct long time scale north-south asymmetric variation, the structure of the atmospheric circulation is, in a

statistical sense, north-south symmetric, consistent with the symmetry of the applied solar flux.

Considering the characteristics of the north-south variation, we examine case $\Omega 0.75$ as representative of Type-III, where the north-south asymmetry appears as a quasi stationary structure that persists throughout the 1000 days of the temporal average. As shown in Fig. 8d, northern (southern) high latitudes are occupied by high (low) pressure throughout the averaging period. The north-south asymmetric features discussed below are naturally reversed in the time period when the surface pressure in the northern (southern) hemisphere is low (high). We also note that the north-south asymmetric atmospheric circulation features develop also in GCM experiments with higher horizontal resolution (T42 and T85), although they appear in slightly different ranges of Ω^* (see Appendix A), so we believe their emergence itself is insensitive to model resolution.

The time mean structure of the atmospheric circulation in case $\Omega 0.75$ is shown in Fig. 9. The deep westerly flow along the equator (Fig. 9b and c), and the associated eastward advection of water vapor (Fig. 9d and g) resulting in a warm belt along the equator in the night hemisphere (Fig. 9h), are features similar to those in Type-II (Fig. 6). However, except for the distribution of evaporation, which is strongly constrained by insolation as was discussed for Type-II, most of the off-equatorial features exhibit north-south asymmetry in contrast to the north-south symmetry in Type-II. Northern (southern) high latitudes are covered with surface high (low) pressure (Fig. 9a). The low pressure area in the day hemisphere also exhibits north-south asymmetry; the low pressure center in the southern hemisphere is much more intense than its counterpart in the northern hemisphere. Being in geostrophic balance with the pressure gradient around the polar pressure anomalies, north-easterly (north-westerly) wind prevails at the surface in northern (southern) mid latitude (arrows in Fig. 9a). This brings dry (moist) air into the mid latitudes of the day (night) hemisphere (Fig. 9g) crossing the day-night boundary at $\lambda = 180^\circ$, inducing the

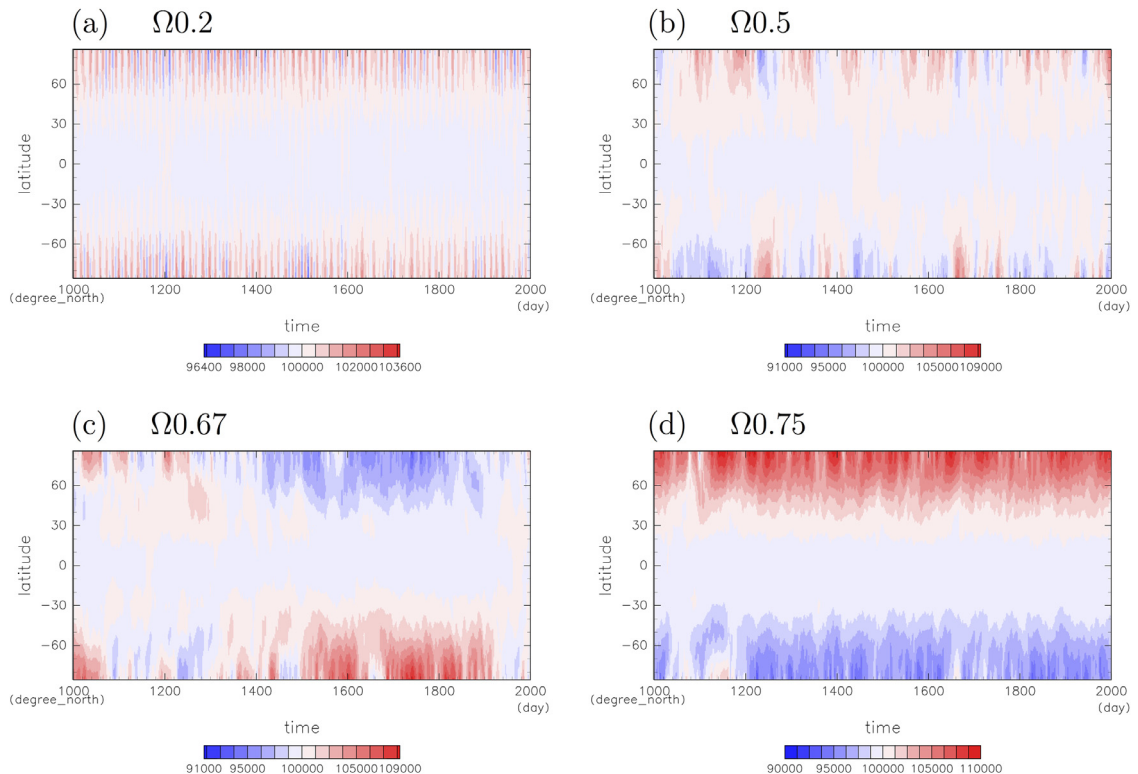


Fig. 8. Latitude–time distribution of zonal mean surface pressure [Pa] for (a) $\Omega 0.2$, (b) $\Omega 0.5$, (c) $\Omega 0.67$, and (d) $\Omega 0.75$.

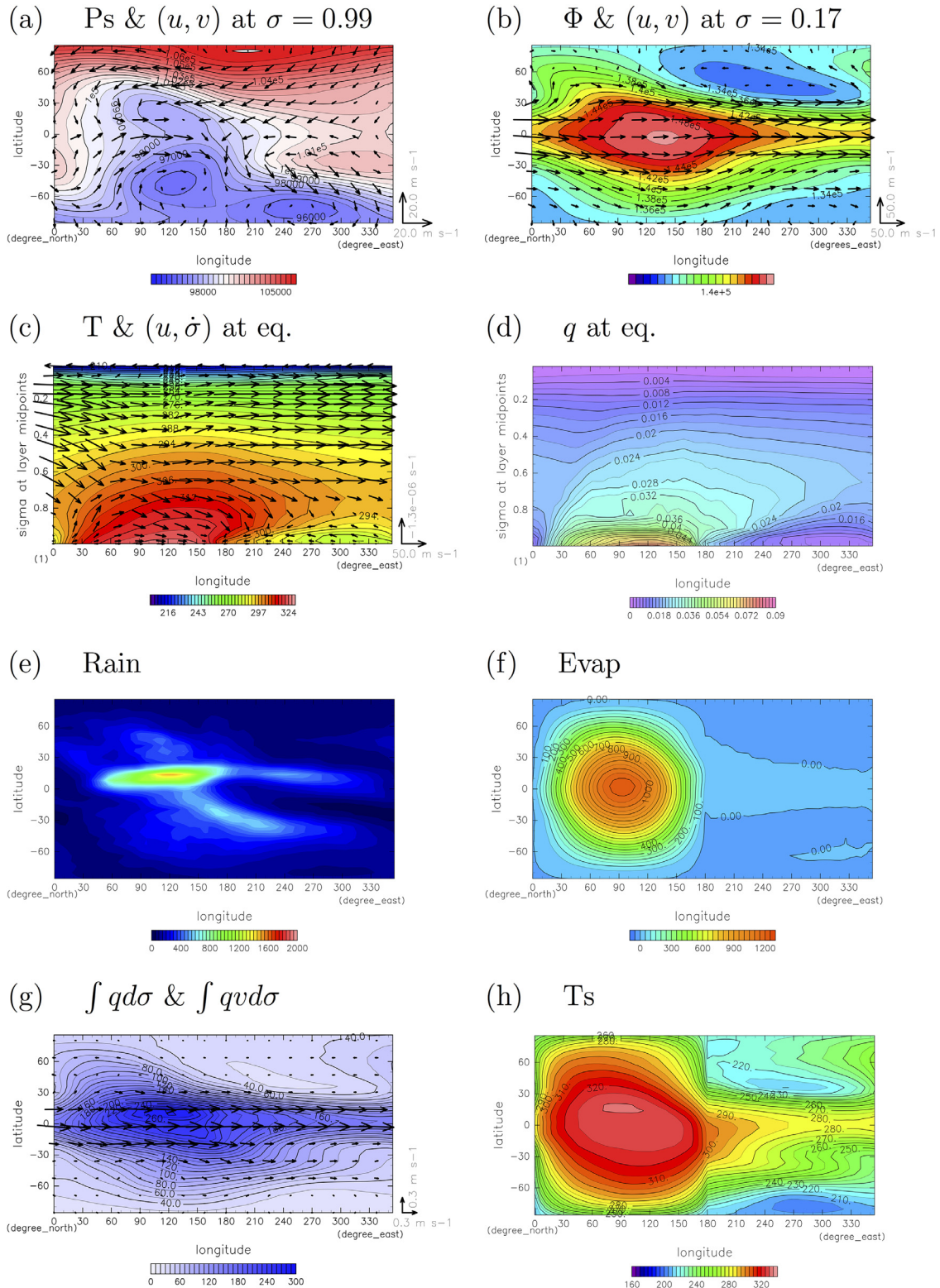


Fig. 9. Same as Fig. 6 but for case $\Omega 0.75$, except that the unit vector of vertical wind in (c) is $1.3 \times 10^{-6} \text{ s}^{-1}$.

north-westward (south-eastward) development of the mid-latitude precipitation zone (Fig. 9e) and the north-south asymmetry of surface temperature in both the day and night hemispheres (Fig. 9h) through the anomaly in downward thermal radiation.

Two additional features characterize the north-south asymmetry. First, the westerly region extends farther poleward in the

southern hemisphere than in the northern hemisphere (Fig. 10a), where intense baroclinic disturbances develop (not shown here), presumably transporting westerly momentum downward. Second, there is a baroclinic zonal wavenumber one feature (Fig. 9ab) which has markedly north-south asymmetric meridional phase tilt (Fig. 10b); the phase lines tilt from northwest to southeast in

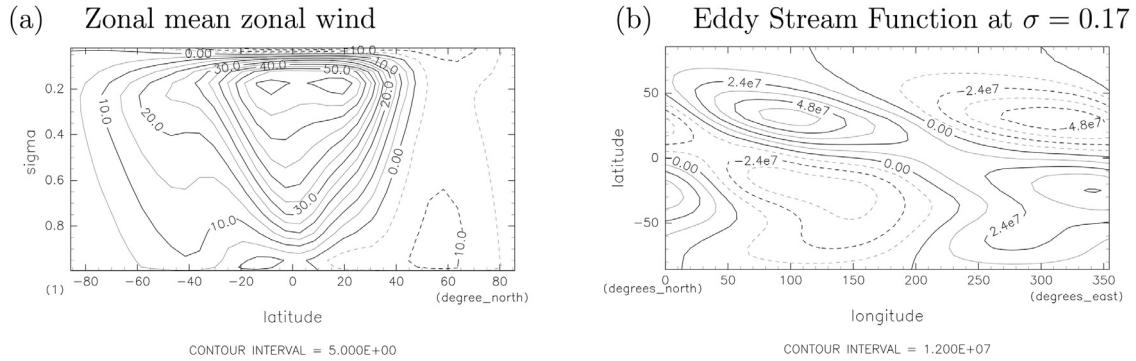


Fig. 10. Structure of the atmosphere averaged from day 1000 to day 2000 for case $\Omega 0.75$: (a) zonal mean zonal wind, and (b) eddy stream function at $\sigma = 0.17$.

a wide latitudinal zone from the northern high latitudes ($\phi \sim +70^\circ$) to southern mid latitudes ($\phi \sim -40^\circ$), crossing the equator. The phase tilt of the zonal wavenumber one feature, which implies southward transport of westerly momentum from northern to southern hemispheres, presumably contributes to driving the mid-latitude westerly jet in the southern hemisphere noted above (Fig. 10a).

According to our preliminary analysis (not shown here) of the vorticity sources following the formulation of Sardeshmukh and Hoskins (1988), the meridionally tilted wavenumber one feature seems to be forced jointly by tropical and extratropical precipitation (Fig. 9e); the heating near the subsolar point, which is distributed mainly in the northern tropics around $(\lambda, \phi) = (120^\circ, +12^\circ)$, can be regarded as an excitation source of a Rossby wave that contributes the northern half of the wavenumber one structure. Meanwhile the latent heating associated with the precipitation band in southern mid latitudes distributed around $(\lambda, \phi) = (180^\circ, -30^\circ)$, can be regarded as an excitation source of a Rossby wave that contributes the southern half. Upward cascade of baroclinic eddies developing in the westerly jet could also contribute to the southern half. The distribution of mid-latitude precipitation seems to be, in turn, induced by the north-south asymmetry of moisture flux associated with surface pressure as described in the previous paragraph. Combining these features, the north-south asymmetry may possibly be maintained through a positive feedback loop, so that the asymmetry tends to have long life time. Quantitative examination of the dynamics of this possible feedback loop remains for future studies.

4.4. Type-IV : mid-latitude westerly jets (case $\Omega 1.0$)

The Type-IV atmospheric circulation structure is found over the entire large- Ω branch for $\Omega^* \gtrsim 0.7$, and is characterized by somewhat Earth-like mid- to high- latitudes westerly jets. This is similar to the structures obtained by Merlis and Schneider (2010) and Edson et al. (2011) with $\Omega^* = 1$, although several points of difference can be noted (See Section 6.1). We examine case $\Omega 1.0$ as a representative case of Type-IV.

The time mean structure of the atmospheric circulation in case $\Omega 1.0$ is shown in Fig. 11. The mid latitudes are occupied by westerly winds through the whole depth of the troposphere (Fig. 11a and b). The low latitudes are occupied by easterly wind, but only in the upper troposphere. The lower tropospheric circulation along the equator (Fig. 11c) is more strongly controlled by the day-night contrast; zonal wind near the surface converges to form the upward motion at the subsolar point, and diverges around the antisolar point compensated by the broad downward motion. In the off-equatorial latitudes, latitudinal tilting of zonal wavenumber one wave features are notable, but these have generally baroclinic ver-

tical structure, in contrast to the barotropic Rossby wave in Type-II. Polar regions are covered with deep low pressure areas.

The precipitation and water vapor distributions are more complicated than those on the small- Ω branch. Precipitation (Fig. 11e) is most intense in a zonally aligned V-shaped region extending from the equatorial point $(\lambda, \phi) \sim (110^\circ, 0^\circ)$ to $(\lambda, \phi) \sim (30^\circ, \pm 25^\circ)$, loosely overlapping the low pressure area in the western part of the day hemisphere (contours in Fig. 11a). The wings of the V-shaped precipitation region intrude into the night side from the regions around $\phi = \pm 25^\circ$ at $\lambda = 360^\circ$. There is also a pair of zonally elongated precipitation zone in the higher latitudes, which start at $(\lambda, \phi) \sim (45^\circ, \pm 45^\circ)$ and extend to $(\lambda, \phi) \sim (330^\circ, \pm 80^\circ)$ on the night side. The distribution of column integrated water vapor content roughly follows that of precipitation (Fig. 11g), but the areas of greatest moisture content are located far from the equator, poleward of the high-latitude parts of the equatorial V-shaped strong precipitation area at $(\lambda, \phi) \sim (50^\circ, \pm 30^\circ)$.

The distribution of night side surface temperature (Fig. 11h) closely follows that of the atmospheric water vapor content (Fig. 11g) as in the cases on the small- Ω branch. However, reflecting the complex structure of humidity, temperature varies longitudinally; it is warmer to the east along $\phi \sim \pm 30^\circ$, whereas it is warmer to the west along $\phi \sim \pm 50^\circ$. Also the distribution of surface temperature on the day side is affected by the distribution of water vapor content; the highest surface temperature appears at $(\lambda, \phi) \sim (80^\circ, \pm 40^\circ)$, the locations that are quite far from the subsolar point and below the belts of large water content (deep blue colors of Fig. 11g). The values of surface temperature at the subsolar and antisolar points are lower than the respective values in Types -II or -III (Fig. 4a and b), resulting from the reduction of atmospheric water content compared to those cases.

5. Day-night energy transport

5.1. Dependence on Ω^*

In this section, we examine how day-night energy transport changes with Ω^* , responding to the considerable variation of the atmospheric circulation structure described in the previous section. We analyze OLR on the night side, F_{OLR} , day-night dry static energy transport, \mathcal{T}_{sens} , and day-night latent energy transport, \mathcal{T}_{lat} , which, in equilibrium states, satisfy the energy balance of the night side:

$$\mathcal{T}_{sens} + \mathcal{T}_{lat} - 2\pi R_p^2 F_{OLR} = 0. \quad (3)$$

\mathcal{T}_{sens} and \mathcal{T}_{lat} are calculated assuming the approximate balances of heat and moisture budgets in the night side atmosphere, which are

$$2\pi R_p^2 (F_{SLR} + F_{sens} - F_{OLR} + LP) + \mathcal{T}_{sens} = 0, \quad (4)$$

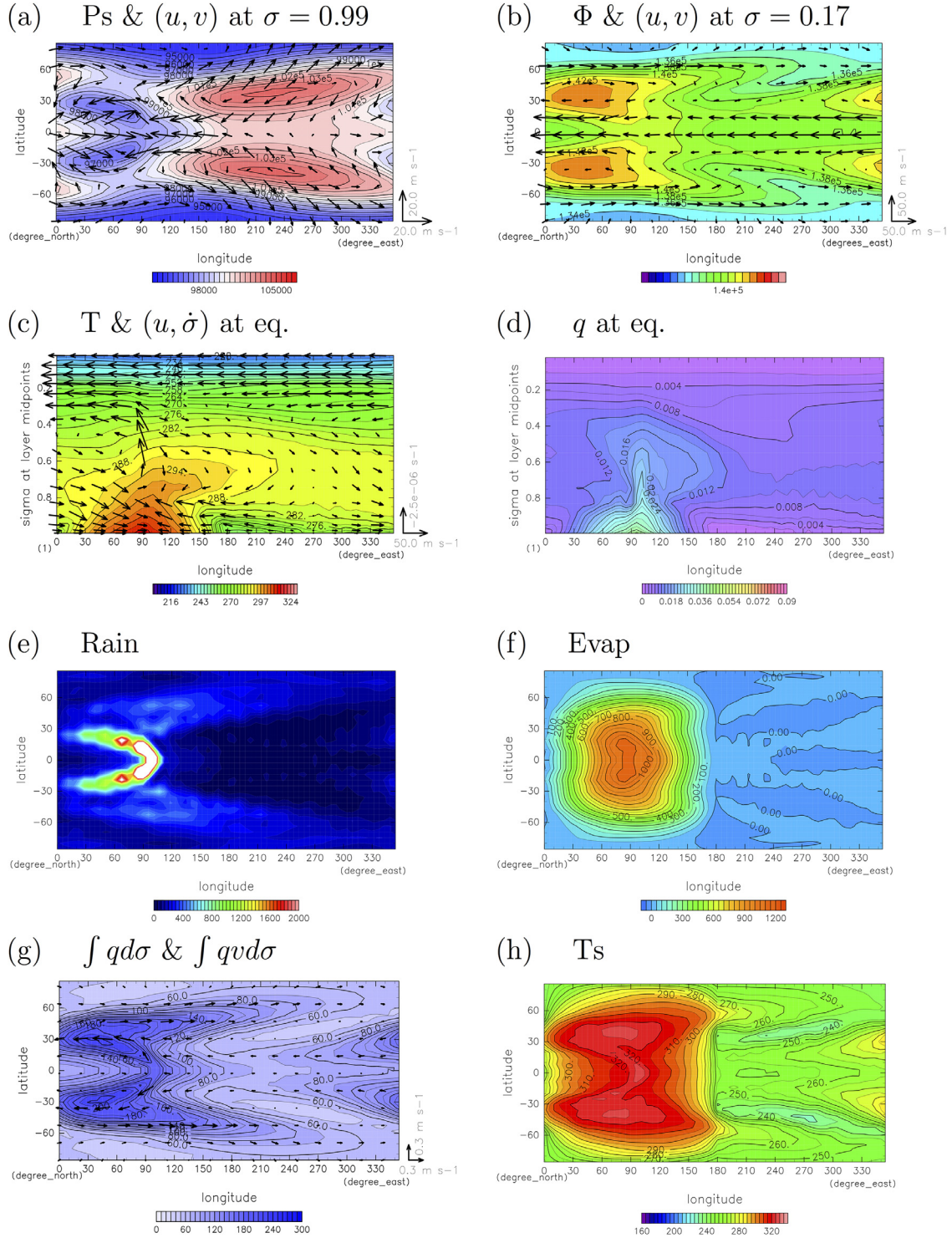


Fig. 11. Same as Fig. 9 but for case $\Omega_1.0$ except that unit vector of the vertical wind in (c) is $2.5 \times 10^{-6} \text{ s}^{-1}$.

$$2\pi R_p^2 (F_{evap} - P) + \mathcal{T}_{lat}/L = 0, \quad (5)$$

where F_{evap} is surface evaporation flux, F_{SLR} is net upward long-wave radiation flux at the surface, F_{sens} is surface sensible heat flux, P is precipitation, and L is latent heat of water vapor. All of the terms are 1000-day mean values spatially averaged over the night side.

Fig. 12a shows Ω^* dependences of F_{OLR} , $\mathcal{T}_{sens}/(2\pi R_p^2)$, and $\mathcal{T}_{lat}/(2\pi R_p^2)$. All 10 runs are plotted for each value of Ω^* . The

most remarkable feature is that total energy transport is almost unchanged regardless of the branch of the solution and the value of Ω^* , while the partition into \mathcal{T}_{sens} and \mathcal{T}_{lat} changes. For $\Omega^* \sim 0$, where the Type-I structure appears, \mathcal{T}_{lat} is negligible, as atmospheric water vapor content is very small (Fig. 5g). As Ω^* increases and the Type-II structure appears, \mathcal{T}_{lat} rapidly increases, but \mathcal{T}_{sens} decreases correspondingly, keeping the sum of the two (F_{OLR}) almost unchanged. The increase of \mathcal{T}_{lat} results from the development of the deep broad westerly wind (Fig. 6b and c) together with the increase of moisture in the day hemisphere (Fig. 6d). Further

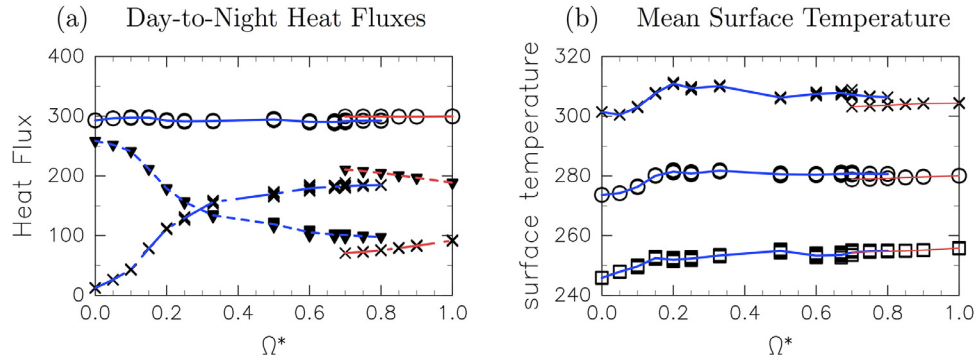


Fig. 12. (a) Ω^* dependences of outgoing longwave radiation on the night side, F_{OLR} (\circ), day-night dry static energy transport per unit area, $\mathcal{T}_{sens}/(2\pi R^2)$ (\blacktriangledown), and day-night latent energy transport per unit area, $\mathcal{T}_{lat}/(2\pi R^2)$ (\times). Units are [W m^{-2}]. All 10 runs for each Ω^* case are plotted. Blue and red lines represent ensemble averages for the small- Ω and the large- Ω branches, respectively. (b) Same as (a) but for global mean (\circ), day side mean (\times), and night side mean (\square) of surface temperature [K]. (For interpretation of the references to colour in this figure legend, the reader is referred to the web version of this article.)

increase of \mathcal{T}_{lat} and decrease of \mathcal{T}_{sens} continue for larger Ω^* as the Type-III with north-south asymmetric variability appears. \mathcal{T}_{lat} exceeds \mathcal{T}_{sens} at $\Omega^* = 0.33$ and \mathcal{T}_{lat} reaches about twice \mathcal{T}_{sens} at the large- Ω end of the small- Ω branch ($\Omega^* = 0.8$). Still, the sum of the two (F_{OLR}) is kept almost constant. At the transition from the small- Ω branch to the large- Ω branch around $\Omega^* \sim 0.75$, \mathcal{T}_{lat} suddenly reduces by about half. Nevertheless, an equally abrupt increase of \mathcal{T}_{sens} means that total heat transport changes only a little. The decline of \mathcal{T}_{lat} at the transition results from the associated disappearance of the broad westerly wind at low latitudes. The type-IV structure has a pair of deep mid-latitude westerly jets blowing through the day and night sides (Fig. 11b), but they cannot transport as much water vapor as the broad equatorial westerly wind in the Type-II or Type-III cases, because the water vapor mixing ratio in the mid latitudes is smaller than in the lower latitudes. The variation of total day-night energy transport is less than 2% over the wide range of Ω^* , while the atmospheric circulation structure varies considerably. Day-night total energy transport scarcely depends on the atmospheric circulation structure.

We have already seen in Fig. 4b that surface temperature at the antisolar point changes greatly with the change of Ω^* . This seems perplexing, since day-night total energy transport is almost constant. However, if we examine the hemispherically averaged temperature, the change is only modest. Fig. 12b shows Ω^* dependences of surface temperature averaged over the night side, the day side, and the whole globe. The range of the variation of night side average temperature is around 10 K, which is much smaller than the variation at the antisolar point of almost 50 K (Fig. 4b). This results from the compensation between the temperature variations in the lower and higher latitudes; in Type-II and Type-III, surface temperature in the low latitudes including the antisolar point is high, while regions of low surface temperature appear in the higher latitudes associated with the large amplitude Rossby waves (Fig. 3b–m). The remaining modest changes of averaged temperatures can be explained mainly by the change of mean column water vapor content.

5.2. Moist atmosphere radiation limit constraint

As described in the previous subsection, the total amount of day-night energy transport is found to be insensitive to the change of Ω^* and to the associated change of atmospheric circulation structure. The invariance of day-night total energy transport is equivalent to the invariance of day side OLR, because the day-night total energy transport is equal to the difference between the day side OLR and the incident solar flux; the latter is constant in the present study. It has been recognized that, in the framework of a

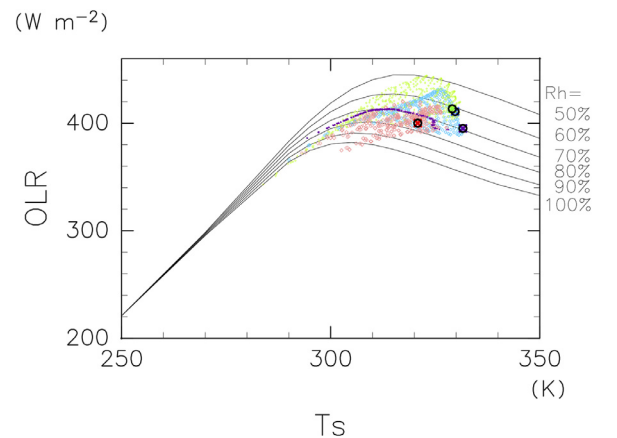


Fig. 13. Relationships between surface temperature and OLR obtained by the GCM and by the one-dimensional (vertical) radiative-convective equilibrium model. The GCM results are shown as colored dots: purple, light blue, green, and pink dots indicate runs $\Omega^*0.20, 0.15, 0.75$, and 1.0 , respectively. Data are from the grid points in the $120^\circ \times 120^\circ$ rectangular region centered on the subsolar point. Crosses in black circles indicate the values at the subsolar point. Black lines are the one-dimensional model results with tropospheric relative humidity of (in order from the top) 50, 60, 70, 80, 90, and 100%, respectively. (For interpretation of the references to colour in this figure legend, the reader is referred to the web version of this article.)

one-dimensional radiative convective equilibrium model, the value of OLR from the atmosphere on a water covered planet can not exceed the radiation limit. In the following, we attempt to understand the invariance of day-night energy transport in relation to the constraint on the day side OLR from the radiation limit of a moist atmosphere.

Fig. 13 shows the relationship between surface temperature and OLR on the day side obtained by the present GCM calculations superposed on the relations obtained by the one-dimensional radiative convective equilibrium model described in Section 4 of Ishiwatari et al. (2002) with several specified values of tropospheric relative humidity. The relationship between surface temperature and OLR is sampled at the grid points within the $120^\circ \times 120^\circ$ rectangular region centered on the subsolar point from the run for each Ω^* described in the previous section.

In all the GCM runs, the maximum values of OLR are between 400 and 430 W m^{-2} , and lie under the values of the radiation limits in the one-dimensional calculation, given that the values of relative humidity averaged over the troposphere on the day side of the GCM runs are within the range 60–80%. Moreover, in each of the GCM results, the relationship between surface temperature and OLR roughly follows those obtained in the one-dimensional calculations. These results imply that the day side OLR in the

present GCM calculations is constrained by the radiation limit of a moist atmosphere on a water covered planet. Now recalling that the system is in a statistically equilibrium state, the amount of day-night total energy transport should be equal to the difference between the incident solar flux and the radiation limit of a moist atmosphere. The results of our GCM calculations indicate that the change in atmospheric circulation structure associated with the change of Ω^* does not modify drastically the mean value of atmospheric humidity, and hence does not affect the value of the radiation limit. This explains the general insensitivity of day-night energy transport to Ω^* obtained in the present GCM calculations.

6. Concluding remarks

6.1. Summary of results and comparison with previous studies

Numerical experiments are performed using a cloud-free, swamp aquaplanet GCM with a gray absorption coefficient for longwave radiation and with the Earth's solar constant. The value of planetary rotation rate normalized by the Earth's value, Ω^* , is varied from 0 to 1. For all Ω^* cases, statistically equilibrium states are obtained; the runaway greenhouse state does not emerge. The circulation structures obtained are classified into four types: Type-I characterized by day-night convection, Type-II characterized by a broad equatorial westerly jet and a stationary Rossby wave, Type-III characterized by a long time scale north-south asymmetric variability, and Type-IV characterized by a pair of mid-latitude westerly jets. Types-I, II, and III evolve continuously from one to another as Ω^* increases, constituting one branch of the solution referred to as the small- Ω branch, whereas Type-IV belongs to a different branch referred to as the large- Ω branch (Fig. 4). For $0.7 \leq \Omega^* \leq 0.8$, multiple equilibrium states emerge; both Type-III and Type-IV are allowed. The dependence of the amount of day-night energy transport on Ω^* is analyzed. It is confirmed that the amount is large enough to prevent the day side atmosphere from entering a runaway greenhouse state. Moreover, the amount is found to be almost insensitive to Ω^* despite the drastic change in the structure of the atmospheric circulation, although the partition into latent and sensible energy transports varies. Day side OLR in the experiments is analyzed and compared with the values obtained with a one-dimensional radiative convective model. The results strongly suggest that day side OLR is constrained by the radiation limit of a moist atmosphere; the details of the circulation structure do not greatly change atmospheric humidity, so the value of the radiation limit is unchanged. This explains the invariance of day-night energy transport, as it is equal to the difference between incoming solar flux and day side OLR. The former is a constant prescribed amount in this study, and the latter is constrained by the radiation limit.

It should be useful to re-examine the circulation characteristics obtained in previous studies from the present viewpoint, since this study has performed a more complete investigation on their sensitivity to Ω^* than previous studies. The “slowly rotating regime” and the “rapidly rotating regime” identified by Merlis and Schneider (2010) presumably correspond to the small- Ω branch and the large- Ω branch in the present study, respectively. However, the correspondence is not certain because they present the horizontal distributions of atmospheric variables for only two values of Ω^* . Circulation structures similar to those of Type-I and Type-IV are obtained for those two values of Ω^* , but it remains unclear whether they obtained atmospheric structures similar to Type-II and Type-III. The dependence of the circulation structure on Ω^* obtained by Edson et al. (2011) can be compared with the results of the present study with more confidence. They observed two separate branches of solutions with multiple equilibria, and solutions with planetary waves of zonal wavenumber one super-

posed on broad westerly wind in the low latitudes for intermediate values of Ω^* . These features are similar to those obtained in the present study.

However, more careful comparison suggests a few differences. One is the difference of the directions of the zonal mean equatorial upper tropospheric wind obtained on the large- Ω branch. It is easterly in the present study, whereas it is westerly in Edson et al. (2011), at least in their “dry” experiment; the structure of the low to mid-latitude Rossby response in the upper troposphere implies that it is also westerly in their “aquaplanet” case, although its intensity and structure is unclear.¹ This difference may originate from the difference in the distribution of precipitation: the maximum of rainfall seems to be located at the equator in the case of $\Omega^* = 1$ of Edson et al. (2011), judging from the figures showing the distribution of cloud cover and the meridionally averaged latent heat flux convergence, whereas it is located in the subtropics in the present study, driving equatorward flow in the upper troposphere (not shown). The difference in precipitation distribution may arise from the differences in the GCM setups used by Edson et al. (2011) and the present study, namely the treatment of oceanic heat transport: they include linear oceanic heat transport, whereas we do not. The fact that Merlis and Schneider (2010), where oceanic heat transport is not included, obtains subtropical maxima of day side precipitation and easterly upper tropospheric zonal mean wind similar to ours supports the speculation. Another difference is in the ranges of planetary rotation rates allowing the multiple equilibria; it is around $\Omega^* = 0.2$ in Edson et al. (2011), but around $\Omega^* = 0.75$ in the present study. Part of the difference originates from our use of rather low horizontal resolution, T21; with T42 and T85, the range shifts to smaller value of Ω (Fig. A.1). Such a difference could be an important issue when considering whether the multiple equilibrium solutions are possible in the habitable zones around M type red dwarf stars, for which $\Omega^* \lesssim 0.5$. The possible sensitivity of the realizability of multiple equilibria to model physics, such as the treatment of cloud, surface albedo, or oceans, will be a focus of future studies.

One of the most novel features in the present experiments may be the global-scale north-south asymmetric variability (Type-III) appearing for a fairly wide range of Ω^* , and its origin remains to be examined in detail. Both Merlis and Schneider (2010) and Edson et al. (2011) do not mention such north-south asymmetric oscillating structures, which suggests that the occurrence of the oscillation may depend on the physical configurations of the experimental design. Both Merlis and Schneider (2010) and Edson et al. (2011) employ a slab ocean with finite heat storage as the surface condition, whereas the swamp condition with zero heat storage is used in the present study. However, oceanic heat storage does not seem to be a critical factor; we repeated several runs of $\Omega 0.75$ employing a slab ocean, and still obtained north-south asymmetric variation essentially similar to that described in Section 4.3. Oceanic heat transport, which Edson et al. (2011) considered, could be more important. Clarification of the conditions for the emergence of the global-scale north-south asymmetric variability, including the possible importance of ocean discussed above, is left for future studies, together with more detailed understanding of the nature and dynamics of the north-south asymmetric variability.

Provided that the north-south asymmetric variability of Type-III in the present study is theoretically permitted, an interesting question would be whether or not such a variability is observationally detectable on exoplanets. In fact, around M9 type red dwarf stars, synchronously rotating habitable planets should have

¹ Edson et al. (2011) presents the maximum values of zonal wind in each of the aquaplanet experiments in Table 3, but does not mention whether it occurs at the equator or not.

$\Omega^* \sim 0.5$ (Kaltenegger and Wesly, 2009), which is in the range for Type-III structure. Typical differences between the northern and southern hemispherically averaged OLRs obtained in our GCM calculations reach about 30 W m^{-2} , which is about 10% of the OLR averaged over the entire day side. Since this difference in OLR is the same order of magnitude as the error in the observation of secondary eclipses of hot-Neptune (e.g., Deming et al., 2009), it might be detectable if the observational accuracy improves by another order of magnitude.

6.2. Mechanics of the broad equatorial jet in type-II

The latitudinally broad equatorial eastward jet in Type-II is similar to those of the synchronously rotating terrestrial planets (Joshi et al., 1997; Edson et al., 2011) and those of the hot Jupiters (Showman and Guillot, 2002; Dobbs-Dixon and Agol, 2013, and others). This universal appearance of equatorial prograde jets in synchronously rotating planetary atmospheres implies the existence of a common underlying mechanism. Showman and Polvani (2010, 2011) argues that the equatorward eddy transport of westerly momentum arising from the superposition of equatorial Kelvin and Rossby waves excited by the day-night contrast of heating is responsible to the appearance of equatorial jets. Preliminary analysis of the present experiments also indicates the importance of the equatorward westerly momentum transport due to stationary eddies, which can be interpreted as generated by Rossby and Kelvin responses to the equatorial thermal forcing as described by Showman and Polvani (2011).

A novel observation in the present study is that the broad equatorial eastward jet is accelerated for a relatively wide range of Ω^* up to or exceeding the speed of the wavenumber one normal mode Rossby wave (Fig. 7). The appearance of the large amplitude normal mode Rossby wave as a near resonance with the zonal mean wind is also noted by Edson et al. (2011) for the case with $\Omega^* \sim 0.2$ in a dry atmosphere of a synchronously rotating planet. Our novel point is that resonant-like behavior is established over much wider range of Ω^* , starting from very small values of Ω^* .

Using a three-dimensional atmospheric model with Earth-like parameters forced by a planetary scale wave-like tropical heat source, Arnold et al. (2012) obtains an abrupt transition of equatorial zonal wind to a westerly speed exceeding that of the propagation of the Rossby wave. Tsai et al. (2014) describes the equatorial acceleration due to a combination of the equatorial Kelvin and Rossby wave responses to thermal forcing, and demonstrates that the longitudinal phase of the Rossby wave is shifted eastward with increasing background westerly wind, and eventually the direction of the westerly momentum flux caused by the combined effect with the Kelvin response is reversed when the background westerly exceeds the resonant speed. The shift of the Rossby response phase is also observed as the difference in circulation pattern between the spin-up and mature periods of the broad equatorial jet formation in the simulation of hot Jupiters by Showman and Polvani (2011). A notable difference between the results of the present study and those for the hot Jupiters of previous studies is that the excited wave here is vertically barotropic rather than vertically propagating. The excitation of the barotropic wave by latent heating can be understood by considering the vertical shear of the broad equatorial westerly jet (e.g., Wang and Xie, 1996) and also the presence of the rigid lower boundary.

It should be kept in mind, however, that the equatorial Kelvin and Rossby responses can only re-distribute westerly momentum within the radius of deformation, and, cannot explain on their own the development of the broad equatorial westerly jet. As the equatorial radius of deformation associated with the barotropic mode concerned is comparable to or larger than the planetary radius, the dominant excitation of barotropic waves is favorable to driv-

ing a meridionally broad equatorial jet. However, there still has to be some other mechanisms to cancel the easterly acceleration at high latitudes, which should compensate for the westerly acceleration around the equator, so as to produce the Type-II wind structure in the present study, whose zonal mean zonal wind is westerly almost everywhere in the middle and upper troposphere (not shown). Downward motion at high latitudes associated with Hadley circulation may contribute to removing the easterly momentum. Detailed investigation of the driving mechanism of the broad equatorial jet, including the effects of various types of transient disturbance, is left for future studies.

6.3. Implications and remaining issues

The lack of sensitivity of the day-night energy transport to the variety of circulation structures demonstrated in the present study has an important implication when considering the habitability of a synchronously rotating planet. Since it ensures that a certain amount of energy is transported from the day side to the night side, relatively warm regions will be maintained at some locations on the night side regardless of Ω^* . In fact, regions with surface temperature warmer than freezing point of water appear on the night side in the present calculation. The location of warm regions on the night side changes with Ω^* ; a warm region appears in the equatorial region to the east of the trailing terminator for the cases on the small- Ω branch, whereas it appears in the mid latitudes to the west of the leading terminator for cases on the large- Ω branch. Based on the location of possible habitable zone for a planetary system discussed by Kaltenegger and Wesly (2009), Ω^* should be generally less than and not very close to one for synchronously rotating habitable exoplanets, which means that the cases on the small- Ω^* branch are more relevant.

It should be emphasized, however, that the insensitivity of day-night energy transport to Ω^* found in the present study is subject to several conditions. We list a few cases below as examples where the insensitivity could be broken. First, when the incident solar flux is small and the day side temperature is not warm enough to raise OLR to the radiation limit of a moist atmosphere, the value of the day side OLR, and therefore day-night energy transport, shall not be constrained by the radiation limit. Second, in contrast, when the incident solar flux is so large that the anticipated amount of day-night energy transport exceeds the amount that can escape from the night hemisphere to space at the radiation limit of a moist atmosphere, the day-night energy transport will differ from that determined by the values of incident solar flux and OLR constrained by the radiation limit on the day side. In this situation, a runaway greenhouse state is expected to occur, where day-night energy transport is also regulated by the radiation limit, but an increase of atmospheric temperature must be considered. Third, when the amount of water on the planetary surface is so small that it is difficult to establish the radiation limit of a moist atmosphere, energy transport may depend considerably on Ω^* . In such situation, i.e., “a land planet”, the change of circulation pattern may even influence whether a statistically equilibrium state is possible (Abe et al., 2010).

Clouds, which are not considered in the present study, may well modify the thermal and dynamical aspects of the present results. Yang et al. (2013) performs a GCM experiment with cloud effects on synchronously rotating planets with increased solar constant. They show that equilibrium states can be obtained with values of the solar constant larger than those for the non-tidally locked case. However, they do not investigate the possible relationship between the emergence of the runaway greenhouse effect and the radiation limit. We have been investigating the latter point in a numerical study, and will report the results in the near future.

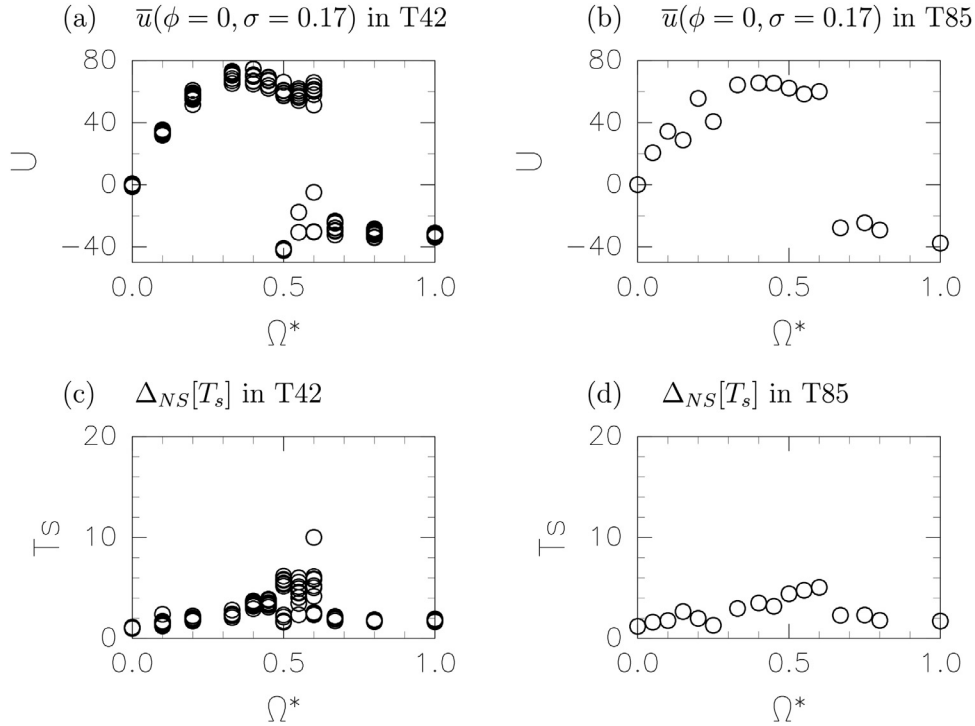


Fig. A.1. (a), (b) Same as Fig. 4c but for the T42 model (a) and T85 model (b), and (c), (d) same as Fig. 4d but for the T42 model (c) and T85 model (d).

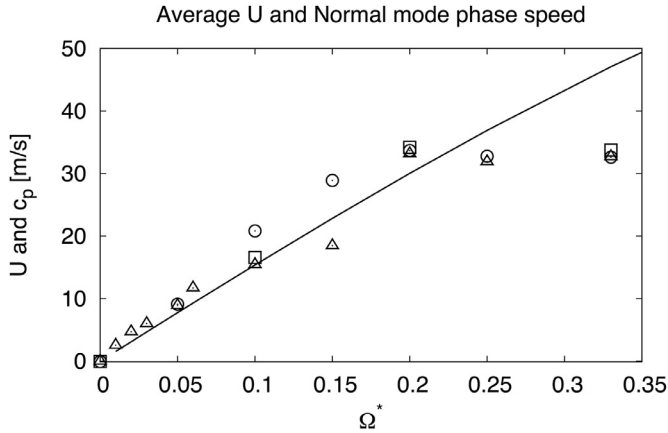


Fig. A.2. Same as Fig. 7, but showing values for horizontal resolutions of T42 (squares) and T85 (triangles) in addition to those for T21 (circles).

Finally, the dynamics of the ocean is undoubtedly an important element to be examined when considering the habitability of synchronously rotating exoplanets. Hu and Yang (2014) performs a series of climate simulation using a coupled atmosphere-ocean model with parameters following Gliese 581g. They find that the ocean can contribute greatly to the day-night hemisphere energy transport and that the partition of the heat transport into the atmospheric and oceanic transports varies considerably depending on the atmospheric CO_2 concentration and the incident short wave flux from the central star. The inclusion of a dynamically active ocean may possibly affect the insensitivity of day-night energy transport to Ω^* . This issue remains as a focus of future studies.

Acknowledgments

Two anonymous reviewers are sincerely acknowledged for carefully reading the original manuscript and providing many help-

ful comments. This study was supported by MEXT KAKENHI Grant Number JP23103003 of Ministry of Education, Culture, Sports, Science and Technology, Japan, and JSPS KAKENHI Grant Numbers JP20540223, JP24340016, JP25400219, JP25800264 and global COE program "Foundation of International Center for Planetary Science" of the Japan Society for the Promotion of Science. A part of calculations were performed by the SX8R of the Institute of Space and Astronautical Science supercomputer system, Japan Aerospace Exploration Agency. Resolution tests of numerical integrations used the SX series of Center for Global Environmental Research, National Institute of Environmental Studies, Japan. We used the software developed by Dennou Ruby Project (<http://www.gfd-dennou.org/library/ruby/>) for simulations, analyses, and drawings.

Appendix A. Dependence on resolution

Because of the large number of experiments required to examine the Ω^* dependence of circulation structures, including the possibility of multiple equilibrium solutions, the horizontal resolution of the GCM used in this study is limited to T21. In this appendix, we check the resolution dependence of the results, by briefly describing the results obtained in models with higher resolution, T42 and T85, focusing on some of the features that may be resolution sensitive. For T42, we have performed 10 runs for each of several selected values of Ω^* . For T85, only one run was performed for each values of Ω^* . In a qualitative sense the main results, namely the existence of the four types of solutions, are not sensitive to the model's resolution, as shown below. Figs. A.1a and A.1b show the upper tropospheric zonal mean zonal wind at the equator for various values of Ω^* in the T42 and T85 models, respectively; for T42, all runs for each Ω^* are plotted. These figures share the main features seen with T21 resolution (Fig. 4c): there are two branches of solutions, and the equatorial zonal wind velocity for each Ω^* is insensitive to the resolution. And, at least in the T42 model, the two branches coexist over a range of Ω^* giving multiple equilibria, although the values of Ω^* with multiple equilibria are about 0.1 smaller than in the T21 model. In the case of

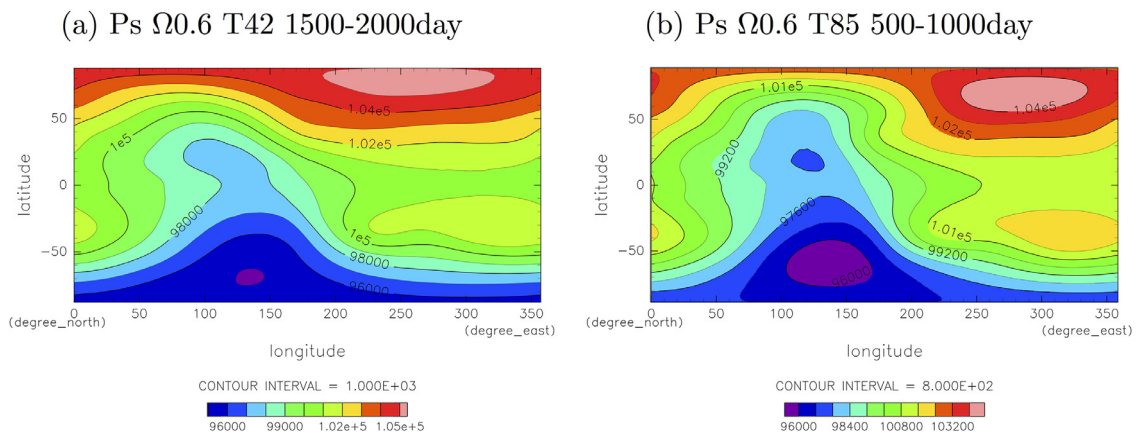


Fig. A.3. Mean surface pressure distributions for $\Omega^* = 0.6$ in the T42 model (a) and T85 model (b) for 500 days during which high (low) pressure occupies the north (south) pole.

the T85 model, as we can only perform one run for each Ω^* , the existence of multiple equilibria cannot be confirmed. However, the overall behavior is not inconsistent with that in T42; the value of Ω^* for the upper end of the small Ω branch is the same.

Fig. A.2 shows the values of mass weighted zonal mean wind speed for different values of Ω^* obtained in the runs with T21, T42 and T85 resolutions, compared with the intrinsic phase speed of the Rossby wave normal mode. In a qualitative sense, we can confirm the main features described in Section 4.2; i.e., the mass weighted zonal mean wind speed closely follows or slightly exceeds the Rossby wave phase speed for $0.0 \leq \Omega^* \leq 0.2$, and levels off for larger Ω^* . The only slight exception is $\Omega^* = 0.15$ in T85, where the zonal mean wind is decelerated by transient disturbance whose nature is unclear.

Figs. A.1c and A.1d show the measure of the north-south asymmetry of surface temperature defined by Eq. 2 for various values of Ω^* in the T42 and T85 models, respectively; for T42, all runs for each Ω^* are plotted. Compared to the corresponding figure for T21 resolution (Fig. 4d), the degree of north-south asymmetry seems to be weaker in higher resolution models. Still, we can identify features largely free from resolution dependence: the monotonic increase of the degree of north-south asymmetry on the small- Ω branch, and the smaller degree of north-south asymmetry on the large- Ω branch. The temporal scales of the north-south asymmetric variability are of the same order of magnitude for all model resolutions (not shown). The spatial structure of the north-south asymmetric variability in Type III, i.e., toward the large- Ω^* end of the small- Ω branch, is also common to all model resolutions. Fig. A.3 shows the horizontal structures of surface pressure in the T42 and T85 models for $\Omega^* = 0.6$ averaged for 500 days during which high (low) pressure occupies the north (south) pole. A comparison with Fig. 9a showing the structure of the variability for $\Omega^* = 0.75$ in the T21 model confirms that all resolutions share the same major features, such as the longitudes of the low pressure area in the southern day hemisphere and the high pressure area in the southern night hemisphere.

References

- Abe, Y., Abe-Ouchi, A., Sleep, N.H., Zahnle, K., 2010. Habitable zone limits for dry planets. *Astrobiol.* 11, 443–460. doi:10.1089/ast.2010.0545.
- Arnold, N.P., Tziperman, E., Farrell, B., 2012. Abrupt transition to strong superrotation driven by equatorial wave resonance in an idealized GCM. *J. Atmos. Sci.* 69, 626–640.
- Deming, D., Seager, S., Miller-Ricci, E., Clavin, M., Lindler, D., Greene, T., Charbonneau, D., Laughlin, G., Ricker, G., Latham, D., Ennico, K., 2009. Discovery and characterization of transiting super earths using an all-sky transit survey and follow-up by the james webb space telescope. *Publ. Astron. Soc. Pacific* 121, 952–967. doi:10.1086/605913.
- Robbs-Dixon, I., Agol, E., 2013. Three-dimensional radiative hydrodynamical simulation of the highly irradiated short-period exoplanet HD 189733b. *Mon. Not. R. Astron. Soc.* 435, 3159–3168. doi:10.1093/mnras/stt1509.
- Edson, A., Lee, S., Bannon, P., Kasting, J.F., Pollard, D., 2011. Atmospheric circulations of terrestrial planets orbiting low-mass stars. *Icarus* 212, 1–13. doi:10.1016/j.icarus.2010.11.023.
- Heng, K., Vogt, S.S., 2011. Gliese 581g as a scaled-up version of earth: atmospheric circulation simulations. *Mon. Not. R. Astron. Soc.* 415, 2145–2157. doi:10.1111/j.1365-2966.2011.18853.x.
- Hu, Y., Yang, J., 2014. Role of ocean heat transport in climates of tidally locked exoplanets around m dwarf stars. *Proc. Natl. Acad. Sci. USA* 111, 629–634. doi:10.1073/pnas.1315215111.
- Ishiwatari, M., Nakajima, K., Takehiro, S.I., Hayashi, Y.-Y., 2007. Dependence of climate states of gray atmosphere on solar constant: From the runaway greenhouse to the snowball states. *J. Geophys. Res.* 112, D13. doi:10.1029/2006JD007368.
- Ishiwatari, M., Takehiro, S., Nakajima, K., Hayashi, Y.-Y., 2002. A numerical study on appearance of the runaway greenhouse state of a three-dimensional atmosphere. *J. Atmos. Sci.* 59, 3223–3238. doi:10.1175/1520-0469(2002)059<3223:ANSOAO>2.0.CO;2
- Joshi, M.M., 2003. Climate model studies of synchronously rotating planets. *Astrobiol.* 3, 415–427. doi:10.1089/153110703769016488.
- Joshi, M.M., Haberle, R.M., Reynolds, R.T., 1997. Simulations of the atmospheres of synchronously rotating terrestrial planets orbiting m dwarfs: Conditions for atmospheric collapse and the implications for habitability. *ICARUS* 129, 450–465. doi:10.1006/icar.1997.5793.
- Kaltenegger, L., Weslly, T.A., 2009. Transits of earth-like planets. *Astrophys. J.* 698, 519–527. doi:10.1088/0004-637X/698/1/519.
- Kasahara, A., 1976. Normal modes of ultralong waves in the atmosphere. *Mon. Wea. Rev.* 104, 669–690. doi:10.1175/1520-0493(1976)104<0669:NMOUWI>2.0.CO;2
- Longuet-Higgins, M.S., 1968. The eigenfunctions of laplace's tidal equations over a sphere. *Phil. Trans. Royal Soc. London A: Math. Phys. Eng. Sci.* 262, 511–607. doi:10.1098/rsta.1968.0003.
- Louis, J.-F., Tiedtke, M., Geleyn, J.-F., 1982. A short history of the PBL parameterization at ECMWF. *Workshop on Planetary Boundary Layer Parameterization*. 59–80, ECMWF, Reading, UK.
- Manabe, S., Smagorinsky, J., Strickler, R.F., 1965. Simulated climatology of a general circulation model with a hydrologic cycle. *Mon. Wea. Rev.* 93, 769–798. doi:10.1175/1520-0493(1965)093<0769:SCOAGC>2.3.CO;2
- Merlis, T.M., Schneider, T., 2010. Atmospheric dynamics of earth-like tidally locked aquaplanets. *J. Adv. Model. Earth Syst.* 2 (Art. #13), 17. doi:10.1029/JAMES.2010.2.13
- Nakajima, S., Hayashi, Y.-Y., Abe, Y., 1992. A study on the “runaway greenhouse effect” with a one dimensional radiative convective equilibrium model. *J. Atmos. Sci.* 49, 2256–2266. doi:10.1175/1520-0469(1992)049<2256:ASOTGE>2.0.CO;2
- Sardeshmukh, P.D., Hoskins, B.J., 1988. The generation of global rotational flow by steady idealized tropical divergence. *J. Atmos. Sci.* 45, 1228–1251. doi:10.1175/JAS-D-14-0235.1.
- Showman, A.P., Guillot, T., 2002. Evolution of “51 pegasus b-like” planets. *Astrophys. J.* 385, 156–165.
- Showman, A.P., Polvani, L.M., 2010. The matsuno-gill model and equatorial superrotation. *Geophys. Res. Lett.* 37. doi:10.1029/2010GL044343.
- Showman, A.P., Polvani, L.M., 2011. Equatorial superrotation on tidally locked exoplanets. *Astrophys. J.* 738, 71. doi:10.1088/0004-637X/738/1/71.
- Showman, A.P., Wordsworth, R.D., Merlis, T.M., Kaspi, Y., 2013. Atmospheric circulation of terrestrial planets. *Comp. Climatol. Terr. Planets* 1, 277–326.

- Torres, G., Kipping, D.M., Fressin, F., Caldwell, D.A., Twicken, J.D., Ballard, S., Batalha, N.M., Bryson, S.T., Ciardi, D.R., Henze, C.E., Howell, S.B., Isaacson, H.T., Jenkins, J.M., Muirhead, P.S., Newton, E.R., Petigura, E.A., Barclay, T., Borucki, W.J., Crepp, J.R., Everett, M.E., Horch, E.P., Howard, A.W., Kolbi, R., Marcy, G.W., McCauliff, S., Quintana, E.V., 2015. Validation of 12 small kepler transiting planets in the habitable zone. *Astrophys. J.* 800 (99), 24. doi:[10.1088/0004-637X/800/2/99](https://doi.org/10.1088/0004-637X/800/2/99).
- Tsai, S.-M., Dobbs-Dixon, I., Gu, P.-G., 2014. Three-dimensional structures of equatorial waves and the resulting super-rotation in the atmosphere of a tidally locked hot jupiter. *Astrophys. J.* 793, 141. doi:[10.1088/0004-637X/793/2/141](https://doi.org/10.1088/0004-637X/793/2/141).
- Von Bloh, W., Bounama, C., Cuntz, M., Franck, S., 2007. The habitability of super-earth in gliese 581. *Astron. Astrophys.* 476 (3), 1365–1371. doi:[10.1051/0004-6361:20077939](https://doi.org/10.1051/0004-6361:20077939).
- Wang, B., Xie, X., 1996. Low-frequency equatorial waves in vertically sheared zonal flow. part i: Stable waves. *J. Atmos. Sci.* 53, 449–467.
- Wordsworth, R.D., Forget, F., Selsis, F., Millour, E., Charnay, B., Madeleine, J.-B., 2011. Gliese 581d is the first discovered terrestrial-mass exoplanet in the habitable zone. *Astrophys. J. Lett.* 733, L48. doi:[10.1088/2041-8205/733/2/L48](https://doi.org/10.1088/2041-8205/733/2/L48).
- Yang, J., Cowan, N.B., Abbot, D.S., 2013. Stabilizing cloud feedback dramatically expands the habitable zone of tidally locked planets. *Astrophys. J. Lett.* 771, L45. doi:[10.1088/2041-8205/771/2/L45](https://doi.org/10.1088/2041-8205/771/2/L45).